A BIOLOGICALLY REALISTIC MODEL OF FLY ELEMENTARY MOTION DETECTION

by

Ichi Lin

A Thesis Submitted to the Faculty of the

DEPARTMENT OF ELECTRICAL AND COMPUTER ENGINEERING

In Partial Fulfillment of the Requirements
For the Degree of

MASTERS OF SCIENCE

In the Graduate College

THE UNIVERSITY OF ARIZONA

2010

STATEMENT BY AUTHOR

This thesis has been submitted in partial fulfillment of requirements for an advanced degree at the University of Arizona and is deposited in the University Library to be made available to borrowers under rules of the Library.

Brief quotations from this thesis are allowable without special permission, provided that accurate acknowledgment of source is made. Requests for permission for extended quotation from or reproduction of this manuscript in whole or in part may be granted by the head of the major department or the Dean of the Graduate College when in his or her judgment the proposed use of the material is in the interests of scholarship. In all other instances, however, permission must be obtained from the author.

SIGNED: _____
Ichi Lin

APPROVAL BY THESIS DIRECTOR

This thesis has been approved on the date shown below:

_____   _____
Charles M. Higgins   Date
Associate Professor of Neuroscience

3

ACKNOWLEDGEMENTS

seg I would like to thank my friends and family for their love and support, Dr. Charles Higgins for always finding time to address my questions and concerns even during the busiest times, and Jon Dyhr for offering invaluable advices and suggestions throughout my years in graduate school.

I would also like to thank the National Institutes of Health for supporting this research (grant number R01 RR008688-16A1).

TABLE OF CONTENTS

TABLE OF CONTENTS – *Continued*

LIST OF FIGURES

LIST OF FIGURES – *Continued*

ABSTRACT

The motion detection circuitry of the insect visual system is essential for many of the remarkable navigational capabilities displayed by flies, such as target tracking and obstacle avoidance. A computational model of the neuronal circuit responsible for elementary motion detection (EMD) has previously been developed based upon the anatomy and physiology of fly brains. However, this model does not match all the key characteristics observed in neuronal recordings from the fly brain. This thesis adds three computational features to the neuronally-based EMD model to better simulate real properties of the insect visual system and to achieve a better match to the biological data. These features include a realistic model for the optics of the compound eye, a functional model of phototransduction, and a spatial band-pass filtering stage that mimics the properties of visual interneurons and produces motion adaptation features not accounted for by the original model.

CHAPTER 1

Introduction

1.1 Motivation

Much of the fly visual system has been evolutionarily conserved for over three hundred million years (Borst et al., 2002). The success of this system is evident from the existence of over 125 thousand identified and an estimated 125 thousand unidentified fly species (Groombridge, 1992). The survival of a fly is heavily dependent on its ability to forage, mate, and navigate in its visual environment, all of which rely on the information-processing ability of its visual system. For this reason, the fly visual system has been a subject of particular interest to the vision research community in the past 50 years (Hassenstein and Reichardt, 1956; Strausfeld and Nässel, 1981; Yamaguchi et al., 2008).

When a three-dimensional scene is viewed by the compound eye of a fly, the light intensity from the visual environment is sampled by each facet on the eye to form a two-dimensional visual image on the retina. During flight, the pattern of this visual image will change as a result of self-movement (referred to as 'egomotion'), and the motion of moving objects in the environment. The neural circuitry in the visual system computes motion information using the light intensity signals acquired by the retina, and relays this motion information to the central brain for navigational control. Information from egomotion is useful for tasks such as visual course control (Borst and Dickinson, 2003) and object avoidance (Srinivasan et al., 1991), and may include estimates of the distance of the fly from objects, as well as the speed at which it is traveling. Information from motion of moving objects in the environment can be useful for visual tracking during prey pursuit (Collett and Land, 1978; Olberg

et al., 2000).

The extraction of motion information from a time series of sampled two-dimensional images is computationally intensive and involves a complex interactive network of neurons. Several studies have shown similarities between the anatomical structures and computational mechanisms present in mammalian and insect visual systems (Hubel and Livingstone, 1987), implying evolutionary convergence across species. Such convergence suggests that we can use information from flies to understand primate vision. The small size of flies makes them an especially attractive organism to study in comparison to primates. A typical fly brain contains approximately 10^6 neurons while a typical primate brain contains approximately 10^{11} neurons (Strausfeld, 1976; Koch, 1999). In addition, each neuron in the fly brain is individually identifiable. This has allowed each type of neuron to be studied in repeated experiments resulting in a more reliable characterization, which is useful for piecing together the components of the neuronal circuit of interest.

Although several previous studies developed models of the motion-detecting circuitry in flies, most were only concerned with modeling the input-output relationships of the circuitry without consideration of how each component within interacts with one another. Higgins et al. (2004) proposed a neuronally-based motion-detecting model which was developed based upon the functional organization of identified neurons in the insect visual pathways. This model has been further elaborated by Rivera-Alvidrez (2005) to include additional features of motion adaptation observed in fly visual neurons. Nevertheless, the elaborated model was still not able to fully match all the characteristics observed in recordings from visual neurons. In this thesis, we explore three additions to the neuronally-based motion-detecting model, based on observations of the anatomy of the insect visual system. Various types of visual stimuli are presented to the revised model to gauge whether it is able to elicit simulated cell responses comparable to those obtained from electrophysiological recordings.

1.2 Guide to Thesis

In Chapter 2 we start by discussing the previous models of motion detection that are of primary interest to vision researchers. These include the feature-tracking scheme (Section 2.1.1) which computes the velocity of an object in the image by dividing its displacement over elapsed time, the gradient scheme (Section 2.1.2) which computes the velocity at each pixel by using the spatial and temporal derivative of the luminance signals, and the correlation-based scheme (Section 2.1.3) which emerged as a result of studies on the optomotor responses of *Chlorophanus viridis* beetles (Hassenstein and Reichardt, 1956) and computes motion by comparing the signal from one photoreceptor and the delayed signal from a neighboring photoreceptor.

In Section 2.2 we follow with a review of the anatomy of the insect visual pathway, working from the optics, the most superficial layer, inward to the lobula, where directional motion outputs are first computed. Having this background information is important for understanding the visual processes that we are interested in modeling. Section 2.2.1 describes the structure of the compound eye and how light intensity in the visual environment is imaged onto the retina. Section 2.2.2 outlines the conversion of photons into electrical signals and further processing performed to modify these signals in the photoreceptor cells. In Section 2.2.3 and 2.2.4, the neurons which are directly implicated in the motion processing pathway in the fly brain are introduced.

After presenting the relevant information on the anatomy of the insect visual pathway, we describe the neuronally-based model developed by Higgins et al. (2004) in Section 2.3. We show how the neuronal response at each cell level is computationally modeled based on the existing knowledge of each neuron of interest described in Section 2.2. In Section 2.4 we present three features of motion adaptation identified in studies by Harris et al. (2000), which are essential for maximizing information transmission in the nervous system by shifting and rescaling the operating range

of motion-sensitive cells. These features of motion adaptation were, however, not accounted for by the first version of the neuronally-based model. In Section 2.5 we introduce an elaborated neuronally-based model (Rivera-Alvidrez, 2005), which was better able to match the motion-adapted responses observed in neuronal recordings.

The contribution of this thesis to the field of insect vision is described in Chapter 3 and Chapter 4. In Chapter 3 we observe the neuronal interactions in the motion visual pathway at the anatomical level and revise the elaborated neuronally based model to match the results obtained in experiments by Harris et al. (2000) more closely. In Chapter 4 we discuss a number of other additions made to the neuronally based model that simulate real properties of the insect visual system, including the addition of an optics stage and a photoreceptor stage (Chapter 4).

In the final chapter (Chapter 5), we summarize the thesis and discuss possible future work for this project.

1.3   Summary

Most of the previous motion detection models did not account for how motion is actually computed by a biological system. Even in the case of biologically inspired models, most were concerned with only mimicking the input-output behaviors of the neural circuitry implicated in the processing of motion information as a 'black box'. Higgins et al. (2004) developed a neuronally based model which was unique in that each computational element was designed based on the properties of the individual neuron types found in the fly brain. However, this model was not able to produce the key motion adaptation characteristics observed in real motion-sensitive neurons. The elaborations to the model made by Rivera-Alvidrez (2005) were able to address some, but not all, of the these characteristics. In this thesis, we take a closer look at the neuronal interactions in the visual motion pathways of flies and form hypotheses for revising the exisiting computational elements as well as for implementing additional components in the model. We produce simulated cell

responses more comparable to those observed in electrophysiology recordings.

CHAPTER 2

Background

In this chapter, some of the most commonly used motion detection schemes will first be reviewed in Section 2.1 to introduce some important computational concepts involved in motion detection. In Section 2.2 the anatomy of the insect visual pathway will be explained in detail starting from the optics of the compound eye to the level of the central brain. This will provide the reader with sufficient background information to understand the neuronally-based elementary motion detection (EMD) model presented in Section 2.3, which was developed based on the functional organization of identified neurons in the fly visual pathway. In Section 2.4, we will review three separate mechanisms observed in the insect visual system involved in maximizing information transmission. A more recent elaboration of the neuronally based model that accounts for some additional properties which were not addressed in previous implementations of the model will be discussed in Section 2.5.

2.1   Models of Motion Detection

Many different models have been proposed for extracting motion information from the visual image. Of these, three classes of visual motion detection schemes are of primary interest to vision researchers: feature-based schemes (Kramer et al., 1997; Braddick et al., 1980; Tomasi and Kanade, 1991), gradient-based schemes (Buchner, 1984; Horn and Schunck, 1981; Marr and Ullman, 1981), and correlation-based schemes (Hassenstein and Reichardt, 1956; Barlow and Levick, 1965; Adelson and Bergen, 1985; van Santen and Sperling, 1985). Both the feature-based and the gradient-based schemes were developed based on computational theory, while the

correlation schemes were developed from modeling biological visual systems using a mathematical approach.

Studies in the past have concluded that in biological systems motion is computed from local light intensity information by two-dimensional, retinotopically organized arrays (Nakayama, 1985) with the following three requirements (Poggio and Reichardt, 1973; Buchner, 1984; Reichardt, 1987). Firstly, motion computation requires at least two spatially separated inputs. Since motion needs to be represented as a vector, it requires at least two points in space. Secondly, it requires a non-linearity, which allows the preservation of information on the temporal sequence of input signals. And thirdly, motion computation requires an asymmetry to distinguish between motion in different directions when the signals are interchanged between two inputs. All three classes of motion detection schemes discussed below match these requirements in some form or another.

2.1.1   Feature-Based Schemes

In the field of computer vision a 'feature' is a broadly defined term. A feature can refer to a point, an edge, or an object in an image. Feature-based motion detection depends on the identification and location of such features. The direction of motion of a feature is determined by its displacement over time, and its velocity is computed by dividing the amount of displacement by the elapsed time. The "facilitate and sample" method (Kramer et al., 1997) is a simple example of motion detection using feature tracking. This method measured the speed of an edge in a moving image using two photoreceptors of a fixed spacing. When the first photoreceptor is activated by a passing feature, an exponentially decaying function is initiated which is sampled when the second photoreceptor is activated. The value of the sampled function provides the time elapsed between the activations of the two photoreceptors, which combined with the spacing between the two photoreceptors is sufficient to provide an estimate of the speed of the moving feature.

While feature tracking is a popular motion detection method in computer vision research, it offers little insight into the early stages of visual motion processing in biological systems. Several psychophysical and behavioral experiments have shown that various species of insects were capable of detecting motion of visual stimuli without prominent features (Braddick et al., 1980). Other disadvantages include the computational expense of selecting and identifying a feature (Tomasi and Kanade, 1991) as well as the difficulty in continuously tracking a feature in the frames of the image stream, referred to as the correspondence problem.

2.1.2   Gradient-Based Schemes

Gradient-based models are used to compute velocity information by using the spatial and temporal derivatives of the luminance at each pixel in the image. In the case of one-dimensional motion, velocity at each pixel can be determined from the luminance gradient as follows:

$$v = -\frac{I_t}{I_x} = \frac{dx}{dt} \tag{2.1}$$

where v is the velocity of the pattern, and I_t and I_x are respectively the temporal and spatial derivatives of the luminance. This method was originally proposed by Limb and Murphy (1975) and can also be extended to a two-dimensional version (Horn and Schunck, 1981) as follows

$$v = -\frac{I_t}{\sqrt{I_x{}^2 + I_y{}^2}} \tag{2.2}$$

where I_x is the spatial derivative of the luminance along the x-axis and I_y is the spatial derivative of the luminance along the y-axis. However, this method is subject to the *aperture problem* like all two-dimensional motion detection schemes (Nakayama and Silverman, 1988). Since each receptor in a biological system has only a limited visual field, it is as if the receptor is looking through a small window or aperture. Therefore, only motion perpendicular to an edge (i.e. motion along the direction
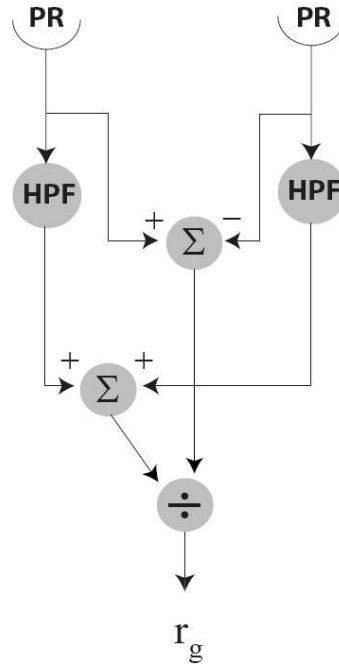
Figure 2.1: A common implementation of gradient-based motion detectors from Buchner (1984). The implementation is described by Equation 2.1. The temporal derivative I_t is approximated using the high-pass filters (HPF) and the spatial derivative I_x is approximated by the subtraction (Σ) of the inputs received by two neighboring photoreceptors (PR).

of the luminance gradient of the image pattern) can be detected. Equation 2.2 will only provide velocity in the orthogonal direction. An implementation of the gradient-based model (see Figure 2.1) uses high-pass filters to model the temporal derivatives and the subtraction between two adjacent sampling points (or photoreceptors) to model spatial derivatives (Buchner, 1984).

The biological plausibility of gradient-based models is questioned due to the presence of the divisive element, since there is no biological evidence supporting the existence of such an operation in the motion pathway. In addition, due to the

spacing between photoreceptors in a biological system, the output of the model is heavily dependent on the spatial frequency of the visual stimulus as observed in motion detection schemes belonging to the classes of gradient-based schemes and correlation-based schemes (Borst and Egelhaaf, 1989). Another disadvantage of this model is that the derivatives enhance noise in the input signal. If the spatial derivative is small, the noise will be further amplified. Also, if the spatial derivative is zero, the divisive element will not be able to produce any meaningful output. While most of these problems have been addressed in an elaborated biologically inspired model (Srinivasan, 1990), a clear pathway in the insect visual system for such a circuit has not yet been identified. Correlation-based models, which will be discussed in the following section, remain the most biologically supported motion detection schemes.

2.1.3 Correlation-based Schemes

There are several versions of correlation-based motion detectors, but one of the most well-known is the Hassenstein-Reichardt (HR) model (1956). The HR model was biologically-inspired and was developed as a result of studies on the optomotor response of *Chlorophanus viridis* beetles. The optomotor response is a turning behavior for gaze stabilization in response to slow wide-field motion in the environment during flight.

These modeling studies also helped guide the discovery of directionally-selective lobula plate tangential cells (LPTCs) in flies which are believed to play an important role in producing optomotor behaviors (Egelhaaf and Borst, 1993). The responses observed from LPTCs were found to match the predictions from the HR model. Operation of the HR model is based on the comparison between the signal from one photoreceptor and the delayed signal from a neighboring photoreceptor (see Figure 2.2). If motion is detected, one of the two multiplicative units will output a large positive value while the other unit outputs a small value. At the output of

the summing unit, one would obtain a positive value for motion in one direction and a negative value for motion in the opposite direction. For instance, if a left-to-right motion stimulus is present, the left photoreceptor will be activated before the right photoreceptor. The inputs to the left multiplicative unit will consist of the delayed signal from the left photoreceptor and the direct signal from the right photoreceptor, while the right multiplicative unit receives the direct signal from the left photoreceptor and the delayed signal from the right photoreceptor. The result is a large positive response (greater coincidence of two signals) at the left arm and a small positive response (less coincidence of two signals) at the right arm, producing a positive final output from the detector. The opposite case of right-to-left motion will produce a negative value at the output. Also note that flickering visual stimuli will yield an output of zero because the summing element will cancel out the equal responses from the two arms in the detector.

An elaboration by van Santen and Sperling (1984) resulted in a version where the point-like receptive fields of the original HR model were replaced with spatial receptive fields, and temporal high-pass filters were added to the outputs of the photoreceptors. These modifications were able to produce outputs that better match data obtained from psychophysical experiments on flies (van Santen and Sperling, 1985). While the HR model is very effective in modeling electrophysiological data accurately, it does not provide insights into the specific neurons and synapses in the visual pathway.

2.2   Optics and Anatomy of the Insect Visual Pathway

Understanding the optics and anatomy of the insect visual system is key to understanding the visual processes that we are interested in modeling. In this section I will provide the necessary background information on the insect visual pathway starting with the optics of the compound eye and the properties of the photoreceptors in Section 2.2.1 and Section 2.2.2, respectively. The optics of the compound
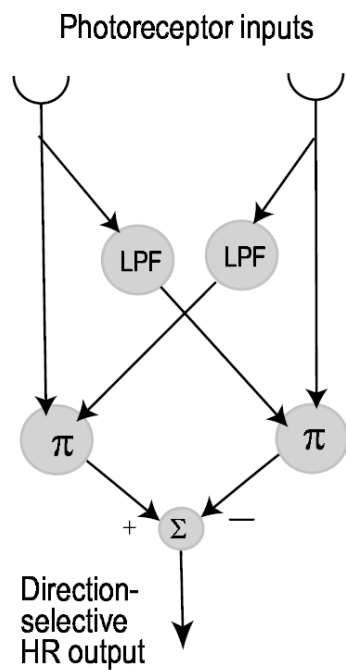
Figure 2.2: The Hassenstein-Reichardt (HR) model. The low-pass filters (LPF) are used as delay elements, such that the input to one photoreceptor is multiplied (π) by the delayed input from its adjacent photoreceptor. Directionally-selective output is then computed by subtracting (Σ) the output of one multiplicative unit from the output of the other multiplicative unit. The output value is a positive for motion in one direction and negative for motion in the opposite direction.

eye serve as an apparatus for light collection while the photoreceptors collect and convert photons into electrical signals. In Section 2.2.3 the unique structural arrangement of the photoreceptor outputs, referred to as neural superposition, will be described. This type of structural arrangement is especially advantageous for vision in low-light conditions. Lastly, the subsequent processing of light information by the three layers of the optic lobes will be discussed in Section 2.2.4. This review will focus on the fly visual system since most of the studies on motion-sensitive visual neurons have been performed on various species of flies.

2.2.1   Optics

Each compound eye of the fly (see Figure 2.3) is composed of thousands of facets referred to as ommatidia, with each ommatidium containing eight photoreceptors (R1-R8) (Beersma et al., 1977). In general the size, density, and the angular spacing between the ommatidia (inter-ommatidial angles) vary across a compound eye. The size of the ommatidia affects the amount of photons collected. Larger ommatidia are more able to collect light compared to smaller ommatidia. The inter-ommatidial angle determines the visual acuity. Regions with smaller inter-ommatidial angles are better at resolving details in an image than regions with larger inter-ommatidial angles. In the frontal region of the fly compound eye one can typically observe a region with larger and more flattened ommatidial facets with smaller inter-ommatidial angles in comparison to other regions of the eye. This specialized grouping of ommatidia is termed the 'acute zone' (Land and Eckert, 1985) and produces an area with high visual acuity and sensitivity (Land, 1981), important for behaviors such as visual tracking (Land and Collett, 1974). On the other hand, the ommatidia found in the lateral regions of the compound eye have larger inter-ommatidial angles and lower visual acuity. It has been suggested by Land and Nilsson (2002) that this decrease in visual acuity is a form of compensation for the fast motion experienced by the lateral regions of the eye during forward flights because it reduces blurring.
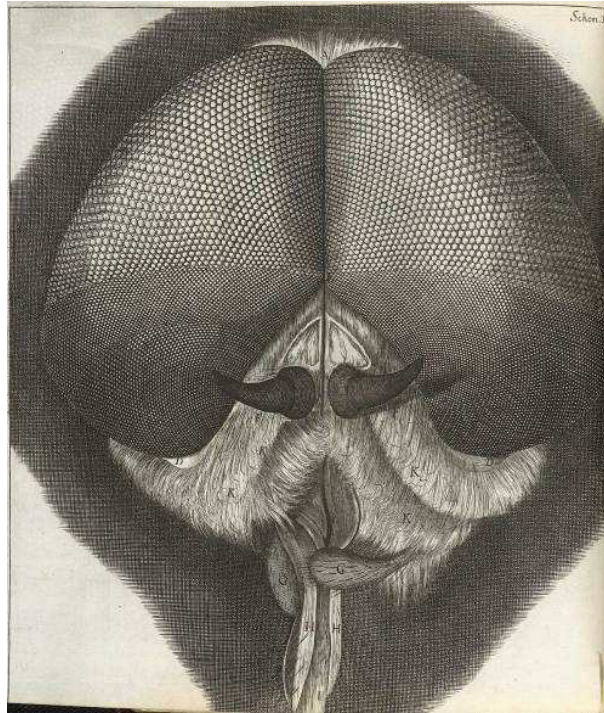
Figure 2.3: The compound eyes of a fly as illustrated by Robert Hooke. Each facet on the surface of a compound eye is referred to as an 'ommatidium'. The density and size of the ommatidia vary across the eye depending on the functional specialization of each part of the eye. Reproduced without permission from Hooke (1665).

Light information is focused by the lens of each ommatidium before it reaches the photoreceptor, where a series of chemical phototransduction processes take place before the processed information is sent to the first layer in the visual ganglia. The three layers – the lamina, the medulla, and the lobula complex – in the visual ganglia are depicted in Figure 2.4 and contain the components of each visual processing unit in the eye referred to as an optic cartridge. An optic cartridge is the set of cells that process each visual sampling unit under a single ommatidium. The optic
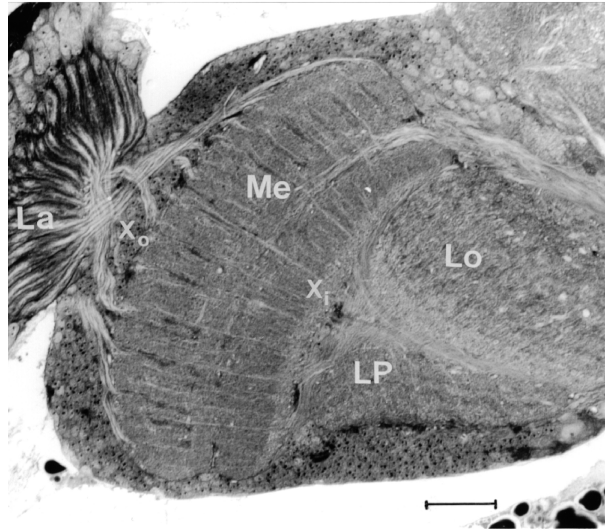
Figure 2.4: Optic lobe of an adult fly. The left side corresponds to the retina side and the right side points to the central brain. La and Me indicate the location of the lamina and the medulla, respectively. LP and Lo indicate the location of the lobula plate and the lobula, respectively, within the lobula complex. X_o denotes the outer optic chiasm connecting the lamina and the medulla. X_i denotes the inner optic chiasm. Reproduced without permission from Tix et al. (1997).

cartridges are said to have a retinotopic organization due to the fact that adjacent optic cartridges are responsible for processing light information from adjacent points in a visual image.

2.2.2   Photoreceptors

During the phototransduction process, photoreceptors measure light through the absorption of photons and convert the intensity information received into electrical signals (Hardie, 2001) at the level of the retina. Light intensity in a natural environment can have a dynamic range up to ten orders of magnitude (from 10^{10} to 10^{20} photons/s/m^2) whereas a typical neuron has a limited dynamic range of approximately one to two orders of magnitude (graded potential of -70 to +50 mV

and a noise level of 5 mV). In order to deal with such a large dynamic range in the inputs, the photoreceptors in most species have developed adaptive mechanisms to accommodate for this varying light intensity (van Hateren and Snippe, 2001). In order to dynamically adjust for the wide range of background luminances, photoreceptors spatially and temporally code for contrast and adjust their gains in order to reduce the signal-to-noise ratio (Juusola et al., 1994). The gain control prevents the photoreceptor responses from saturating at high light levels as well as increases the sensitivity of the photoreceptors to contrast. This type of adaptive mechanism can be computationally described by a transition from a low-pass filter to a band-pass filter as the photoreceptor adapts to variations in the luminance conditions (Jarvilehto and Zettler, 1971).

2.2.3   Neural Superposition

Apposition eyes are the most common form of compound eyes in arthropods. In the majority of apposition eyes, all the photoreceptors within an ommatidium are fused together to form a single light-guiding structure known as a rhabdom (Figure 2.5 *left*). In a typical apposition eye, each rhabdom samples light information from a slightly different angle, such that all eight photoreceptors within a single rhabdom sample light from the same direction (Figure 2.6a). Further studies on neural interconnections in the fly eye led to the discovery of a subclass of apposition eyes referred to as neural superposition eyes (Kirschfeld and Franceschini, 1968). Neural superposition is exhibited by dipteran flies and differs from a normal apposition eye in that each of the eight photoreceptors from within an individual ommatidium projects to a separate "rhabdomere" (Land and Nilsson, 2002) as shown in Figure 2.5 *right*. Each rhabdomere in a single rhabdom samples light information from a different angle (Figure 2.6b). In the lamina layer of the optic lobe, the six outer rhabdomeres (R1-R6), which are involved in motion processing (Yamaguchi et al., 2008), project to neighboring optic cartridges, while the two inner rhabdomeres (R7
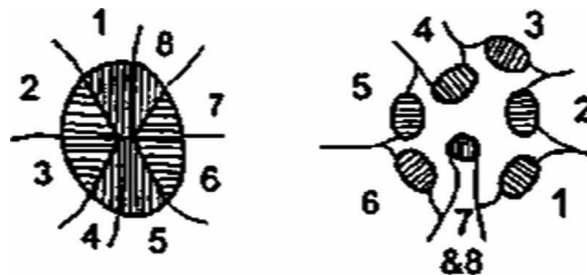
Figure 2.5: Rhabdom of an apposition eye and rhabdomeres of a neural superposition eye. In an apposition eye (*left*) all photoreceptors within an ommatidium are fused together to form a single light guiding structure referred to as a rhabdom. In a neural superposition eye (*right*), each of the eight photoreceptors from within an individual ommatidium projects to a separate 'rhabdomere' such that there are a total of eight rhabdomeres within a rhabdom. Reproduced without permission from Land (1997).

and R8), which are involved in color vision, bypass the lamina and terminate in the medulla (Hardie, 1985). In the end, each optic cartridge receives light information from a given angle contributed by six neighboring ommatidia, which is essential for vision in low-light conditions.

2.2.4 Visual Neurons in the Optic Lobe

As briefly mentioned earlier, the optic lobes consist of three neuropils: the lamina, the medulla, and the lobula complex (Figure 2.4). The lobula complex is further subdivided into two separate neuropils: the lobula and the lobula plate. As visual information travels deeper from the superficial layers of the optic cartridges, the processing of light information becomes increasingly complex and specialized. Simple first-order filterings are first performed at the lamina level to remove redundancy from the visual inputs. As the pre-processed signals reach the medulla, visual information is segregated into pathways which are responsible for different tasks such as the processing of motion and color information. In the lobula, outputs of the

apposition

(a)

neural superposition

(b)
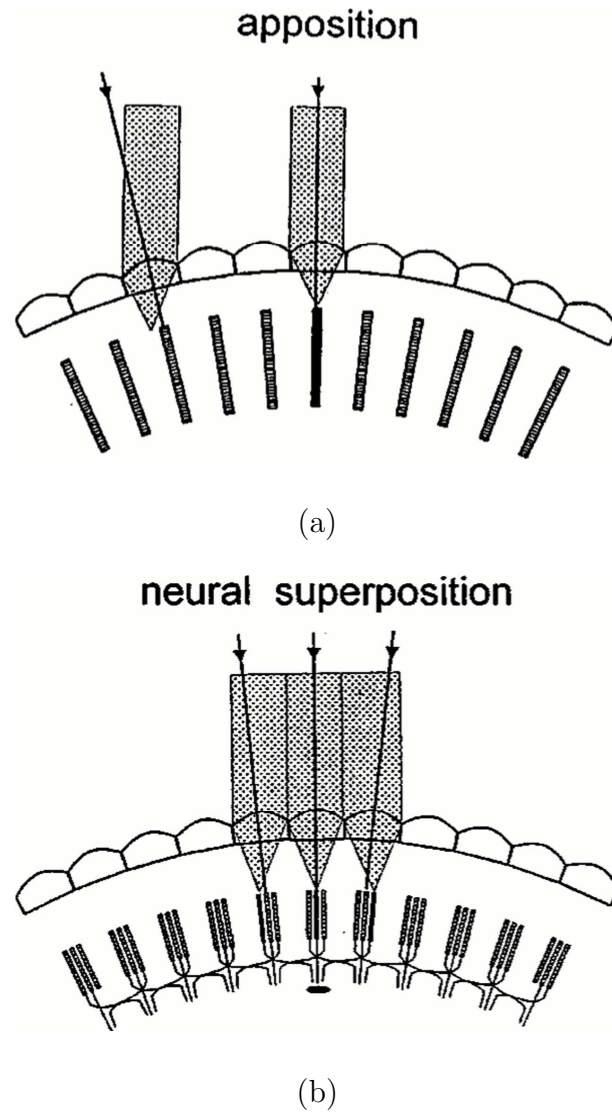
Figure 2.6: Comparison between an apposition eye and a neural superposition eye. The shaded beams represent the light information coming from a point in a distant image and the arrows indicate the optical axes of the ommatidia. In an apposition eye (a) only a single rhabdom (shown in *black*) samples the light information coming from a point, while in a neural superposition eye (b) the light information from the same point is sampled by several rhabdomeres (shown in *black*). Reproduced without permission from Land (1997).

medulla are further refined to extract more specific visual information, which is projected to the central brain for higher-order processing. Although there are a large number of neurons residing in the optic lobes of a fly, we shall focus the following discussion on a subset of neurons which are evolutionarily conserved across many insect species and have been directly implicated in visual motion processing.

The lamina is widely believed to be the site where redundant information in the visual input is discarded through the spatial and temporal high-pass filtering properties of neurons at this level (Laughlin et al., 1987). In addition, in neural superposition eyes, the duplicate visual information from multiple photoreceptors is organized as outlined in Section 2.2.3.

The lamina houses the amacrine cells (AMs), the T1 "basket" cells (T1s), and the lamina monopolar cells (LMCs), among other smaller neurons. The AM cells receive visual signals from the photoreceptors and are believed to play a role in lateral inhibition due to their widespread network of interconnections between neighboring optic cartridges. The T1 cells are post-synaptic to the AM cells (Campos-Ortega and Strausfeld, 1973). Each T1 cell receives AM cell inputs from six neighboring optic cartridges and responds transiently to light with a sign opposite to that observed at the photoreceptor level and with an additional small sustained component (Douglass and Strausfeld, 2005). Out of the five identified types of LMCs (L1-L5), the L2 cells are the most well studied and are believed to be the LMCs most implicated in motion processing. Like AM cells, an L2 cell receives input from a single photoreceptor. L2 cells respond transiently to increasing luminance by hyperpolarizing and show no significant response to sustained illumination (Coombe et al., 1989). Inhibition between neighboring LMCs results in the spatial and temporal interactions that are believed to be key to reducing redundancy in the lamina (Srinivasan et al., 1982).

The axons extending from the lamina undergo the first optic chiasm before they reach the second neuropil in the optic lobe. Within the medulla reside the transmedullary cells (TMs). The terminals of L2 and T1 cells both synapse onto the

dendrites of TM1 cells (Campos-Ortega and Strausfeld, 1973). The TM1 cell level is believed to be the earliest site where *non-directional* motion is detected. Studies by Douglass and Strausfeld (1995) have suggested that TM1 cells respond strongly to motion whereas flickering visual stimuli only elicit weak responses. Another class of TM cells, the TM9 cells, receives inputs from the TM1 cells through a series of complex relays.

Across the second optic chiasm from the medulla is the lobula complex. T5 cells residing in the lobula are believed to be pre-synaptic to lobula plate tangential cells (LPTCs) in the lobula plate (Strausfeld and Lee, 1991). Each T5 cell integrates signals received from TM1 and TM9 cells from neighboring optic cartridges. Studies by Sinakevitch and Strausfeld (2004) have also identified a GABA-immunoreactive interneuron in the T5 dendritic layer which has an inhibitory role at the T5 level. Each optic cartridge has four T5 cells, and each cell of the quartet in an individual optic cartridge extends to each of the four layers in the lobula plate which is sensitive to motion in a different orientation (Buchner et al., 1979). Outputs at this level are considered outputs of the EMD. Since only motion from small regions of the visual field is computed here, the EMDs are considered small-field sensitive. EMD outputs from the lobula are relayed to the lobula plate for further signal integration to extract more motion information. The lobula plate has a wide receptive field (termed wide-field sensitive) and contains approximately sixty identifiable lobula plate tangential cells (LPTCs) in each hemisphere (Hausen, 1982; Hengstenberg, 1982; Eckert and Dvorak, 1983) whose outputs are directionally-selective. Different types of LPTCs can be classified by the orientation which they respond to (e.g. horizontal or vertical motion) and their response mode (spiking, graded response, or both) among other properties (Borst et al., 2002). Out of the LPTCs selective to motion in the horizontal orientation, the centrifugal (CH) cells respond with graded potentials, the cells H1 through H4 have spiking responses, whereas the horizontal-system (HS) cells respond with a mixture of both. Out of the LPTCs selective to

motion in the vertical orientation, the vertical-system (VS) cells respond in a similar manner to the HS cells, while the V1 cells are purely spiking cells. The LPTCs have been the subject of intense study due to their importance in the optomotor response mentioned in Section 2.1.3 during flight control (Hausen, 1984).

2.3   Neuronally Based Model

A model of elementary motion detection was developed by Higgins et al. (2004) based on studies of identified neurons in the fly visual system. Motion responses obtained from this model match those of the HR model. The model predicts the responses of a subset of neurons involved in motion information processing in the fly brain through the three neuropil layers to the lobula plate. In this section we will show how the neuronal response at each cell level is computationally modeled based on the existing knowledge of each neuron of interest described in Section 2.2.4. The model developed by Higgins et al. (2004) is presented in Figure 2.7. It shows the neuronal circuitry and the mathematical computations involved in generating the cell responses in the pathway.

In the lamina layer, the amacrine cell (AM) and the laminar monopolar cell (L2) receive input from the photoreceptors. The AM cell then synapses onto the basket T-cell (T1) and this synapse is modeled with a sign-inverted relaxed high-pass filter (RHPF) since the response is opposite of that of the photoreceptors and contains a small component of low frequencies. The T1 cell response is then computed as the sum of two low-pass filtered neighboring AM cells in the 1-D model (or of six low-pass filtered neighboring AM cells in the 2-D model). The response of the L2 cell is implemented as a sign-inverted high-pass filter (HPF) since no sustained component was observed in previous electrophysiological studies (Coombe et al., 1989). In the medulla layer, the transmedullary cell (TM1) receives inputs from both T1 and L2 and performs summation on these signals. TM1 is non-directionally sensitive, which means that the mean cell responses to motion in all directions are identical. In the
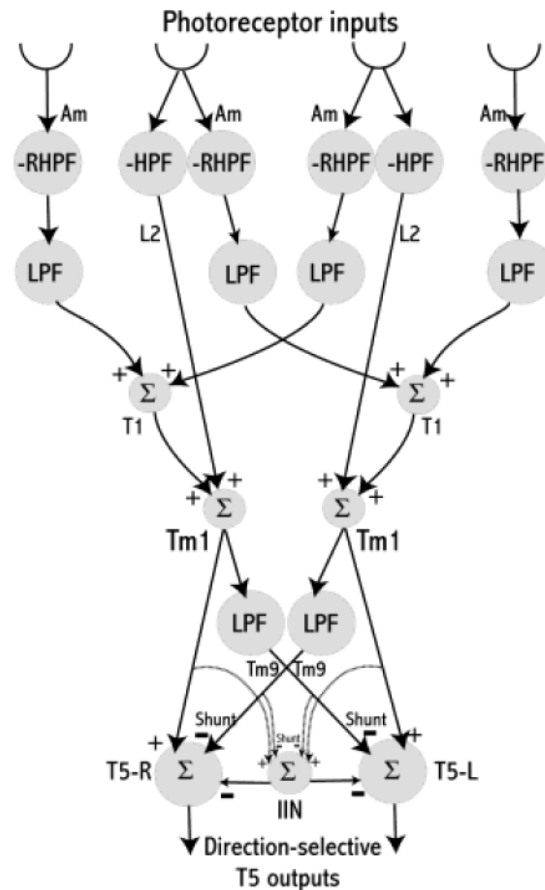
Figure 2.7: The one-dimensional neuronally based model of elementary motion detection. This model as proposed by Higgins et al. (2004) describes the response of each neuron type implicated in motion information processing in the optic lobe, including the amacrine (AM) cells, the lamina monopolar 2 (L2) cells, the basket T-cells (T1), the transmedullary (TM1 and Tm9) cells, and the bushy T-cells (T5). LPF and HPF denote low-pass filters and high-filters, respectively. RHPF stands for a 'relaxed-high pass filter' which represents a high-pass filter that retains a small sustained component. 'Shunt' represents shunting inhibition and the summing operations are represented by Σ.

lobula, the T5 cells receive signals from the TM1 cell and the TM9 cell (modeled as a delayed version of TM1) from the neighboring visual unit. Together, the T5, TM1 and TM9 cells form a Barlow-Levick motion detector (Barlow and Levick, 1965), where TM1 acts as an excitatory input and TM9 acts as an inhibitory input. The T5 cells receive excitatory inputs from one local TM1 cell and a number of neighboring TM1 cells, whose relative orientation to each other determines the preferred-null axis of the T5 cells. Note that the preferred direction refers to the direction of motion which a cell responds maximally to, and the null direction refers to the direction of motion which a cell responds minimally to.

In this model motion is computed in two stages. Non-directional motion is first computed at the TM1 level by comparing a local signal with delayed signals from neighboring optic cartridges. Directional motion then is computed at the T5 level through the special geometric arrangement and non-linear shunting inhibition of the T5 cells by the TM1 and TM9 cells. The model yields comparable results to those from the HR model (see Higgins et al., 2004). However, unlike the HR model, it can be used to further the understanding of the neuronal basis of motion detection since it is based upon the functional organization of identified neurons in the neural circuitry of the insect visual system.

2.4   Motion Adaptation

Motion adaptation is the decrease in the response of cells to sustained motion stimuli. Many species exhibit motion adaptation when viewing images of high velocity. Studies have shown that this type of adaptation is essential for maximizing information transmission in the nervous system (Brenner, 2000) by shifting and rescaling the operating range of motion-sensitive cells (Maddess and Laughlin, 1985). Motion adaptation in the fly visual system has been of much interest due to its similarity to the adaptive mechanisms in the primate visual system (Kohn and Movshon, 2003). When presented with continuous motion stimulation, the LPTCs in the fly optic
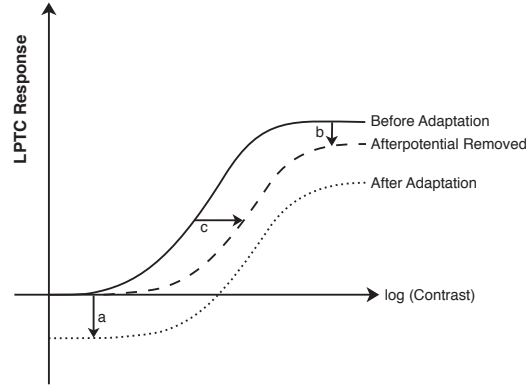
Figure 2.8: The effect of motion adaptation on the mean LPTC cell responses. Afterpotential (*a*) causes the mean LPTC response to decrease uniformly over the entire range of pattern contrasts. When the effect of afterpotential is removed, the effect of the reduction in contrast gain (*c*) that causes the rightward shift of the trace becomes more visible. In such case a higher pattern contrast is necessary to elicit the same amount of LPTC response compared to before adaptation. One can also observe a lower saturation level indicated by *b*.

lobe were observed to have responses which decay over time (Maddess and Laughlin, 1985). It was also discovered that the rate of decay increases with an increase in the temporal frequency of the visual stimulus, and that this adaptive mechanism takes place at the EMD level in the lobula. In a series of experiments performed by Harris et al. (2000), the effects of presenting high-contrast, high-frequency motion stimuli (referred to as strongly adapting stimuli), on the responses of LPTCs were further characterized. Three features of motion adaptation were identified from this study (see Figure 2.8): the after-potential, the reduction in saturation level, and the reduction in contrast gain. Each of these features will be discussed briefly in Section 2.4.1, Section 2.4.2, and Section 2.4.3, respectively.

2.4.1 Afterpotential

Evidence for the effect of an afterpotential in the fly visual system was first discovered by Maddess (1986). After exposure to stationary or slow-moving visual stimuli, the HS cells responded with a reduction in their baseline potentials. It was suggested that the afterpotential might be used to attenuate signals from far-away or slow-moving objects (Maddess, 1986). Others have also proposed the possibility of its role in dynamically adjusting the temporal resolution in the motion pathway in response to varying image velocities (Harris and O'Carroll, 2002). The afterpotential is very similar to the waterfall illusion observed in the human visual system (Tootell et al., 1995), where one experiences the visual illusion of perceiving movement from a still object in one direction after presentation of a moving stimulus in the opposite direction. In flies, this has been suggested to be the result of the imbalance between a pair of mutually antagonistic neurons (sensitive to motion in opposite directions) in the lobula plate when the response of the neuron sensitive to the direction of motion is attenuated (Srinivasan and Dvorak, 1979).

2.4.2 Reduction in Output Range

Recordings from HS cells (Egelhaaf and Borst, 1989) have shown their responses to reach a saturating level as the contrast of the visual stimulus increases. Egelhaaf and Borst (1989) implicated this saturating behavior in the ability of the cells to estimate the temporal frequencies of visual stimuli independent of their contrasts. In the series of experiments performed by Harris et al. (2000), the contrast curves (mean LPTC response versus contrast of motion stimulus) were generated for responses before and after the presentation of a strongly adapting stimulus. A lower saturating level was observed from the contrast curve of post-adapted responses even after the effect of the afterpotential was removed. This reduction in saturating level represents an overall decrease in the output range of LPTC responses. Nevertheless, its effect

in motion adaptation as a whole is very small in comparison to the effects from the afterpotential and the reduction in contrast gain.

2.4.3   Reduction in Contrast Gain

Among the three features of motion adaptation described here, experiments by Harris et al. (2000) showed that the reduction in contrast gain contributes the most to the shift of the contrast-response curve from post-adaptation. This effect was found to be more prominent when the HS cells are adapted to motion than to flicker. In addition, adaptation with motion stimuli in both the preferred and the anti-preferred (180° from the preferred) directions produces a comparable amount of decrease in contrast gain. Even orthogonal motion stimuli elicited a similar response. Since this mechanism does not seem to be directionally-selective, it has been suggested that this process is small-field sensitive and takes place in neurons pre-synaptic to wide-field neurons (Maddess and Laughlin, 1985). This is to be compared to the afterpotential and the reduction in output range, both of which were shown to be activity-dependent as well as directionally-sensitive, and are believed to take place at the level of LPTCs. Harris et al. (2000) explained that the function of the reduction in contrast gain might be to restore sensitivity of the visual pathway to varying contrast levels when the LPTCs are operating near saturation level from high-contrast visual stimuli. However, to optimally avoid saturation of the visual system, Harris et al. (2000) proposed that this mechanism should take place before the saturation mechanism at the TM9 level and reside before the EMD circuitry.

2.5   Elaborated Neuronally Based Elementary Motion Detector Model

The 2004 neuronally based EMD model has been modified in the past few years, enabling it to better match physiological data recorded from LPTCs. In both the HR model and the original neuronally based EMD model, the simulated LPTC responses

increase as the square of the visual input contrast levels. However, this squared response is not biologically possible due to the limited dynamic range of neurons described in Section 2.2.2. In Rivera-Alvidrez and Higgins (2005), a saturating nonlinearity was incorporated into the neuronally based EMD model to produce the contrast saturation observed in LPTCs. In the same set of studies, pattern size saturation was also implemented to reduce the sensitivity of the model to sparseness in the moving visual field due to the varying size of the visual stimuli. In terms of modeling features of motion adaptation, the reduction in contrast gain is of the most interest since out of the three features described in Section 2.4 it was the only one hypothesized to take place at the EMD level. In Rivera-Alvidrez (2005), the reduction in contrast gain discussed in Section 2.4.3 was modeled as a frequency-dependent synaptic depression.

In Rivera-Alvidrez and Higgins (2005), saturating elements were inserted into the neuronally based EMD model at the synapses from the TM1 cells onto the TM9 and the T5 cells, similar to ones used by Egelhaaf and Borst (1989) to produce the contrast saturation in the HR model. The saturating element is denoted by the 'S' in Figure 2.9 and was modeled as a sigmoid function in Equation 2.3:

$$S(x) = A + B \cdot \frac{1}{1 + e^{-C \cdot x}} \tag{2.3}$$

where A, B, and C were set to -0.085, 0.17, and 43, respectively to match electro-physiological data. Pattern size saturation was modeled at the LPTC level where the integration of EMD inputs takes place. This saturation was implemented using the gain control equation (Equation 2.4 below) described in Borst et al. (1995) and Single et al. (1997):

$$V = \frac{E_e g_e + E_i g_i}{g_e + g_i + g_{leak}} \tag{2.4}$$

where E_e and E_i are the excitatory and inhibitory reversal potentials, g_e and g_i are the excitatory and inhibitory conductances, respectively, and g_{leak} is the leakage conductance. In the elaborated model, E_e, E_i were set to 0.4 and -0.3 based on the
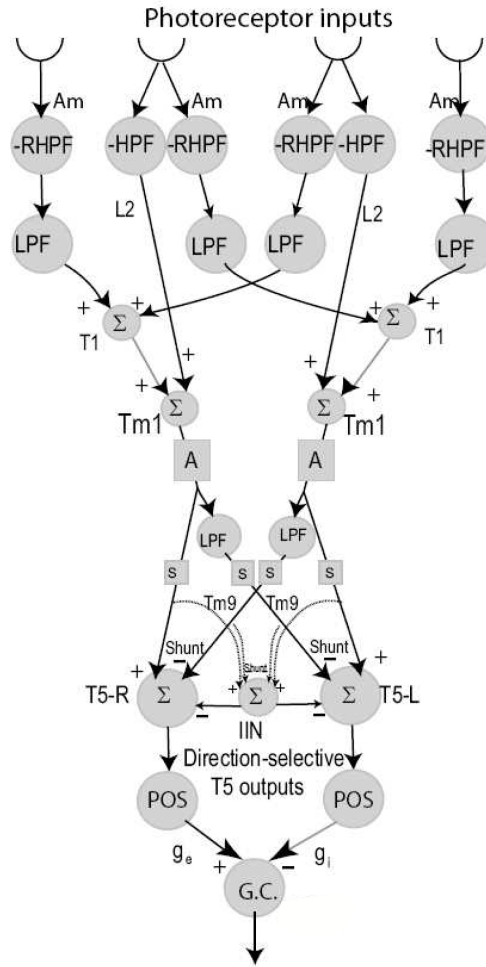
Figure 2.9: The one-dimensional *elaborated* neuronally based model of elementary motion detection. This model from Rivera-Alvidrez (2005) retains all components from the original one-dimensional neuronally based model and incorporates additional computational components including the frequency-dependent synaptic depression at the TM1 level (A), the saturating non-linearity (S) at the inputs to the T5 cells, and the pattern size gain control (G.C.) for the integration of T5 outputs into LPTC responses. 'POS' represents the operation which discards any negative component of the input signal.

description in Single et al. (1997), while the value of g_{leak} was empirically set to 3.5 S. g_e and g_i represented inputs coming from the rectified responses of the preferred-direction T5 unit and the null-direction T5 unit, respectively. The pattern size saturation is denoted by the 'G.C.' (gain control) in Figure 2.9.

Referring to Figure 2.9, Rivera-Alvidrez (2005) implemented the reduction in contrast gain before the contrast saturation ('S' blocks) to restore the contrast sensitivity by decreasing the responses below the saturation level, as suggested by Harris et al. (2000). As previously mentioned, the reduction in contrast gain is non-directionally selective and more prominent when adapted to motion compared to flicker. Therefore the most likely location in the original neuronally based EMD model (refer to Figure 2.7) for this mechanism to occur is at the TM1 level. The TM1 cells respond non-directionally to preferred and null directions as well as to both horizontal and vertical directions. Additionally, TM1 may be capable of differentiating between motion and flicker (Higgins et al., 2004). The mechanism responsible for the reduction in contrast gain is represented by the 'A' (adaptation) blocks in Figure 2.9. The depression of the synaptic responses from the TM1 cells onto the TM5 cells and the TM9 cells was modeled as a frequency-dependent synaptic depression. A depression gain factor was introduced such that the post-synaptic TM1 cell response can be modulated as shown in Equation 2.5.

$$TM1_d = f(t) \cdot D(t_r) + V_{rest} \tag{2.5}$$

where $TM1_d$ is the post-synaptic depression TM1 cell response, $f(t)$ is pre-synaptic TM1 cell response, $D(t_r)$ is the depression gain factor, and V_{rest} is the resting potential of the cell. The value of the depression gain factor decreases when the pre-synaptic TM1 cell response is above its resting potential and rising, and the gain factor increases if the pre-synaptic TM1 cell response is below resting potential and falling. The value of this gain factor $D(t)$ varies between 0 and 1, and is determined

using Equation 2.6:

$$D(t) = \begin{cases} \frac{1}{\frac{1}{D(t_r)}+f(t)\cdot D(t_r)} & \text{if } (\frac{\partial f(t)}{\partial t} > 0 \text{ and } f(t) > 0) \\ \frac{1}{1+(\frac{1}{D(t_d)}-1)\cdot e^{-\frac{(t-t_d)}{\tau_d}}} & \text{otherwise} \end{cases} \qquad (2.6)$$

where t_r represents the time at which the rise of the last positive modulation begins, t_d is the time when the positive modulation ends, and τ_d is the empirically determined time constant of recovery from the synaptic depression.

The implementation of this synaptic depression was able to produce LPTC responses qualitatively similar to those recorded by Reisenman et al. (2003) and displayed a significant reduction in contrast gain after adaptation with motion compared to the responses from before adaptation. Nevertheless, contrast-response curves generated using this elaborated model showed very little difference between the motion-adapted responses and the flicker-adapted responses when compared to data from Harris et al. (2000). As discussed in Section 2.4.3, adaptation to flicker generally produces weaker responses from the HS cells compared with adaptation to motion. When the one-dimensional EMD model was used instead of the two-dimensional version a more pronounced difference between motion-adapted responses and flicker-adapted responses could be observed. This is due to the fact that only two neighboring photoreceptor cells are summed (as opposed to six neighboring photoreceptors in the two-dimensional model) in the computation of the T1 response, therefore reducing its response to flicker compared to motion.

It has been hypothesized that the addition of early visual processing might result in the desirable response through the inhibitory interaction between the different types of AM cells. The next chapter will describe further efforts on modifying this elaborated neuronally based EMD model specifically to produce different amounts of reduction in contrast gain between the motion-adapted responses and the flicker-adapted responses in order to match the results obtained in experiments by Harris et al. (2000) more closely. A number of other additions made to the neuronally

based EMD model that simulate real properties of the insect visual system will also be discussed.

CHAPTER 3

An Improved Model of Contrast Gain Adaptation

In Section 2.5 we learned that the elaborated neuronally-based EMD model was not able to fully produce the difference observed between the motion-adapted contrast-response curves and the flicker-adapted contrast-response curves presented in Harris et al. (2000). In this chapter, we propose the implementation of a center-surround spatial band-pass filter at the amacrine cell level, to suppress the response to flickering stimuli and relatively enhance the response to motion stimuli in order to produce a better match to physiological data. We first present a number of clues from previous studies of fly neuroanatomy providing supporting evidence for this proposed implementation.

As mentioned in Section 2.2.4, the lamina is believed to be the site of redundancy reduction in the insect visual pathway (Laughlin et al., 1987). Studies from Sinakevitch and Strausfeld (2004) suggest that both type 1 amacrine cells (AM1) and type 2 amacrine cells (AM2) have widespread networks such that the response of a single optic cartridge can travel and spread across several levels of neighboring optic cartridges. L2 cells from neighboring optic cartridges do not have connections to one another (Strausfeld and Nässel, 1981), but they exhibit the center-surround spatial antagonism (Srinivasan et al., 1982) found in cells belonging to a spreading network. There is no direct synaptic interaction between amacrine cells and L2 cells, however, both cells are both pre- *and* post-synaptic to the photoreceptor cells (Strausfeld and Nässel, 1981).

Combining these pieces of information, we hypothesize a series of synaptic interactions between the photoreceptor cells, the amacrine cells, and the L2 cells in the lamina as follows. AM1 and AM2 cells receive synaptic inputs from photoreceptor

cells. The signals spread across the network of AM1 cells and the network of AM2 cells, such that each AM1 or AM2 cell represents the weighted sum of its local signals and the signals from its neighboring optic cartridges. An inhibitory interaction between the AM1 and AM2 cells (that could possibly occur at the amacrine cell level or the photoreceptor cell level) results in the subtraction of the AM1 responses from the AM2 responses before the signals reach the L2 cell level. These signals are hypothesized to be communicated back to the photoreceptor cells, which then relay the signals to the L2 cells. We hypothesize that in some way the photoreceptor cells act as the liaison between the AM cells and the L2 cells. It has in fact been widely accepted that the adaptive mechanisms observed in the photoreceptor cells are not intrinsic to themselves, but rather the result of a series of synaptic connections to downstream neurons such as the AM cells and the L2 cells (Juusola et al., 1994).

Based on this hypothesis, we propose that the center-surround spatial filter at the L2 level is composed of the subtraction of a Gaussian spreading network of AM1 cells from a similar spreading network of AM2 cells. The filtered output from this processing by the amacrine cells is relayed to and shared by the L2 cells. To reflect this center-surround spatial filtering in the two-dimensional EMD model, we add a computational module (Figure 3.1) that is mathematically described by Equation 3.1:

$$AM_{out}(i) = [f(i) * g_2] - w \times [f(i) * g_1] \tag{3.1}$$

with

$$g_1(n_1, n_2) = e^{-\left(n_1^2 + n_2^2\right)/2\sigma_1^2}$$
$$g_2(n_1, n_2) = e^{-\left(n_1^2 + n_2^2\right)/2\sigma_2^2}$$

where $AM_{out}(i)$ is the output signal from the amacrine network at the ith frame, $f(i)$ is the two-dimensional array of photoreceptor responses at the ith frame, $*$ denotes the convolution operation, g_1 and g_2 are the spatial Gaussian filters, and w is a scalar weight used for determining the amount of attenuation of the spatial mean

component of the visual stimulus. Each Gaussian filter is normalized such that the sum of the coefficients is equal to 1, to ensure that signals are passed through with unity gain. The subtraction represents the inhibitory interaction between AM1 and AM2 cells. The use of the spatial Gaussian filters g_1 and g_2 represent the spreading networks of AM1 and AM2 cells, respectively. This center-surround-type spatial filter allows the preservation of motion information while eliminating the spatial mean luminance from flickering stimuli by computing the difference between the two Gaussian filters of different widths, σ_1 and σ_2, with σ_1 larger than σ_2. In addition, the value of w can be adjusted between 0 and 1 to control the amount of the spatial mean luminance in the motion pathway, since recorded data from the LPTCs did reflect some responses to flickering visual stimuli. A w of 0 allows the passage of all the spatial mean components while a value of 1 only enables the passage of transient components.

With the addition of the center-surround spatial filter, the artificial saturating elements 'S' from the previous model are no longer sufficient to produce the amount of saturation observed in LPTC electrophysiology data from Egelhaaf and Borst (1989). For this reason, further downstream in the EMD model at the T5 level, the "dirty multiplication" used in Higgins et al. (2004) to represent the T5 cell shunting inhibitory synapse is replaced by the model for synaptic interaction outlined in Koch (1999) to reflect the real biophysics of cells. This implementation is essential for producing simulated LPTC responses with saturating behavior of a close match to those from Egelhaaf and Borst (1989). This interaction between an excitatory synapse and an inhibitory synapse in a passive dendritic tree is described by Equation 3.2:

$$V_s = \frac{g_e E_e \left(\tilde{K}_{es} + g_i \tilde{K}_e^+ \right) + g_i E_i \left(\tilde{K}_{is} + g_e \tilde{K}_i^+ \right)}{1 + g_e \tilde{K}_{ee} + g_i \tilde{K}_{ii} + g_e g_i \tilde{K}^*} \tag{3.2}$$

with

$$\tilde{K}_i^+ = \tilde{K}_{is} \tilde{K}_{ee} - \tilde{K}_{es} \tilde{K}_{ie}$$
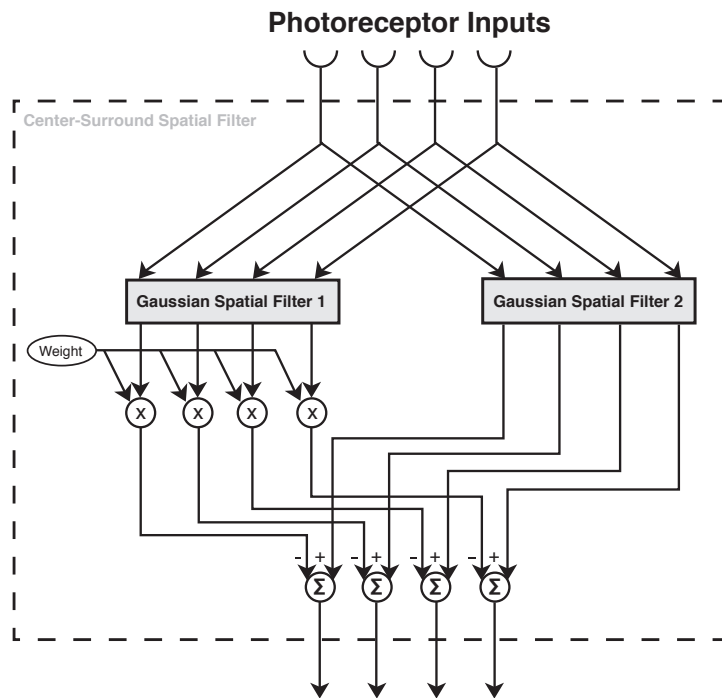
Figure 3.1: Operation of the center-surround spatial filter. This filter computes the difference between two Gaussian filters of different widths. The value of the weight parameter can be adjusted between 0 and 1 to control the amount of spatial mean luminance in the motion pathway. When the weight is equal to 1, the subtraction between the two Gaussian filters eliminates all the spatial mean luminance in the input signals. Smaller values of the weight allow the preservation of more spatial mean luminance in the inputs.

$$\tilde{K}_e^+ = \tilde{K}_{es}\tilde{K}_{ii} - \tilde{K}_{is}\tilde{K}_{ie}$$
$$\tilde{K}^* = \tilde{K}_{ee}\tilde{K}_{ii} - \tilde{K}_{ie}^2$$

where E_m and g_m denote the potential and the conductance of the input, respectively, at location m, $\tilde{K}_{mn}$ denotes the transfer resistance between location m and n, and the subscripts e, i, and s respectively denote the excitatory and inhibitory input locations, and the soma location. Equation 3.2 not only accounts for the biophysics of shunting inhibition but is also able to produce the nonlinearity of contrast saturation explained in Section 2.4.2, without the explicit use of the saturating elements as done in the elaborated neuronally-based EMD model.

To summarize, in our revised EMD model shown in Figure 3.2 the saturating elements ('S' blocks) are removed, the center-surround spatial band-pass filters are added to the AM cell and the L2 cell pathways, and the shunting inhibition at the T5 level is replaced with the biophysical implementation.

3.1 Methods

All experiments from this section were carried out using the revised EMD model shown in Figure 3.2, which includes the center-surround spatial filtering (Equation 3.1), the frequency-dependent synaptic depression at the TM1 level (Equation 2.5) and the pattern size saturation at the LPTC level (Equation 2.4) implemented by Rivera-Alvidrez (2005), and the biophysical shunting inhibition function (Equation 3.2). All temporal filter parameters remained the same as those used in Higgins et al. (2004), except for the low-pass filter immediately following the 'A' block whose time constant has been empirically adjusted to 0.097 s.

In our current model, the reduction in contrast sensitivity was quantitatively matched to that observed in real LPTCs by Harris et al. (2000) by empirically adjusting the w parameter (amount of DC attenuation in Equation 3.1) in the center-surround spatial filter and the τ_d parameter (time constant of recovery in Equa-
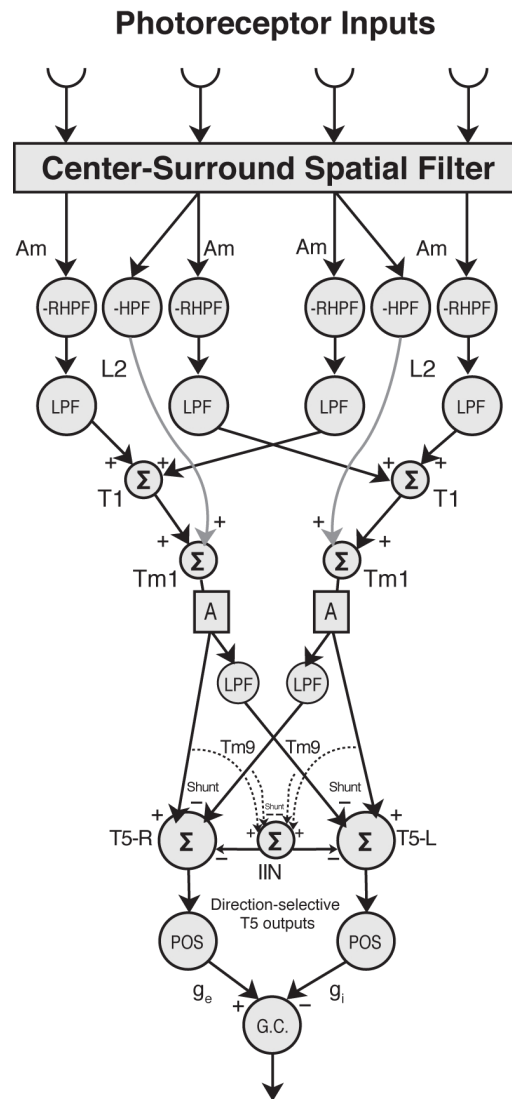
Figure 3.2: The one-dimensional *revised* neuronally based model of elementary motion detection. This model differs from the one shown in Figure 2.9 in a number of ways. (1) The center-surround spatial filters (refer to Figure 3.1 for details) were implemented at the AM and L2 cell level to eliminate the spatial mean luminance in the input signals. (2) The shunting inhibition at the T5 level was replaced with a biophysical implementation outlined in Koch (1999). (3) The sigmoid functions denoted by 'S' blocks in the previous model were removed.

tion 2.6) of the synaptic depression at the TM1 level. The value of w determined the difference in the amount of contrast sensitivity reduction between motion-adapted and flicker-adapted responses. The larger the value of w, the greater the removal of the spatial mean component from the input signals, resulting in a smaller reduction in contrast sensitivity for flicker-adapted responses relative to motion-adapted responses. The value of τ_d affected the amount of reduction in contrast sensitivity for motion-adapted responses, with a larger value of τ_d producing a larger amount of reduction in contrast sensitivity.

Within the center-surround spatial filter (Equation 3.1), the relative weight w between these two filters has been empirically set to be 0.98, in order to produce the desired amount of adaptation to flickering stimuli relative to the amount of adaptation to motion stimuli (see Figure 3.7(a)). The first Gaussian filter g_1 had a σ_1 of 13 pixel units while the second Gaussian filter g_2 had a σ_2 of 4 pixel units. These two values were chosen to match the spatial tuning intrinsic to the EMD model. The kernel size used for both filters was chosen to be 27 pixel units as the minimum to avoid significant artifacts in the filters.

The mechanism accounting for contrast saturation was inherent in Equation 3.2, and the amount of saturation could be adjusted by choosing a value for the K_{ee} parameter (the transfer resistance at the excitatory input) appropriately. A larger value of K_{ee} was used to produce a greater amount of saturation in the contrast-response curve. In Equation 3.2, $\tilde{K}_{es}$, $\tilde{K}_{ee}$, $\tilde{K}_{ei}$, $\tilde{K}_{is}$, $\tilde{K}_{ii}$, $\tilde{K}_{ie}$, and E_e were each empirically set to be 11 MΩ, 65 MΩ, 16 MΩ, 15 MΩ, 100 MΩ, 16 MΩ, and 0.5 arbitrary voltage units, respectively, to match electrophysiological data (Koch, 1999). E_i was set to 0 for shunting inhibitory synapse. g_e and g_i were the rectified excitatory input and the rectified inhibitory input, respectively. In the pattern size saturation function (Equation 2.4), all the parameters remain the same as in Rivera-Alvidrez (2005) except for E_i whose value was adjusted to -0.4.

As expected in a nonlinear system, small changes made to the model can dras-

tically change its responses. To ensure that the basic electrophysiological characteristics modeled by the previous version of the neuronally-based EMD model (see Figure 2.7) were preserved, simulations of experiments from Franceschini et al. (1989), Egelhaaf and Borst (1989), and Coombe et al. (1989) were performed. The protocol used for these experiments were identical to those outlined in Higgins et al. (2004).

All the simulations were performed using the *Matlab* package (The Mathworks, Natick, MA). Each simulation consisted of a 100×100 pixel image (with a 100 Hz frame rate) viewed by a 20×20 hexagonal array of photoreceptors. When generating simulated H1 cell responses for comparison with data from Reisenman et al. (2003), the test stimuli were (as in that paper) composed of square-wave moving gratings with a fixed spatial frequency of 0.41 cycles/optic cartridge, a temporal frequency ranging from 2 Hz to 16.7 Hz, and a pattern contrast between 11% and 95%. Each experiment was repeated for 50 trials to reduce artifacts resulting from the initial spatial phase of the test stimulus. In each trial a uniform stimulus at the mean luminance was shown for 4 s followed by the presentation of the test stimulus for 3 s. Simulated LPTC responses were generated as in Higgins et al. (2004) (see Figure 3.3).

When generating the contrast response curves for comparison with the HS cell responses from Harris et al. (2000), sinusoidal moving gratings as in that paper were used. For each simulation, a test stimulus with a spatial frequency of 0.37 cycles/optic cartridge and a temporal frequency of 5 Hz was presented for the first 1 s, which was followed by the presentation of an uniform stimulus for 500 ms. Then a strongly adapting stimulus (with a high pattern contrast of 95%, a spatial frequency of 0.37 cycle/optic cartridge, and a temporal frequency of 20 Hz) was applied for 4 s immediately followed by the test stimulus again for 1 s. The simulation was repeated for 10 different test stimulus pattern contrasts between 0% and 100%. The simulated mean LPTC response measured between 200 ms and 500 ms following the
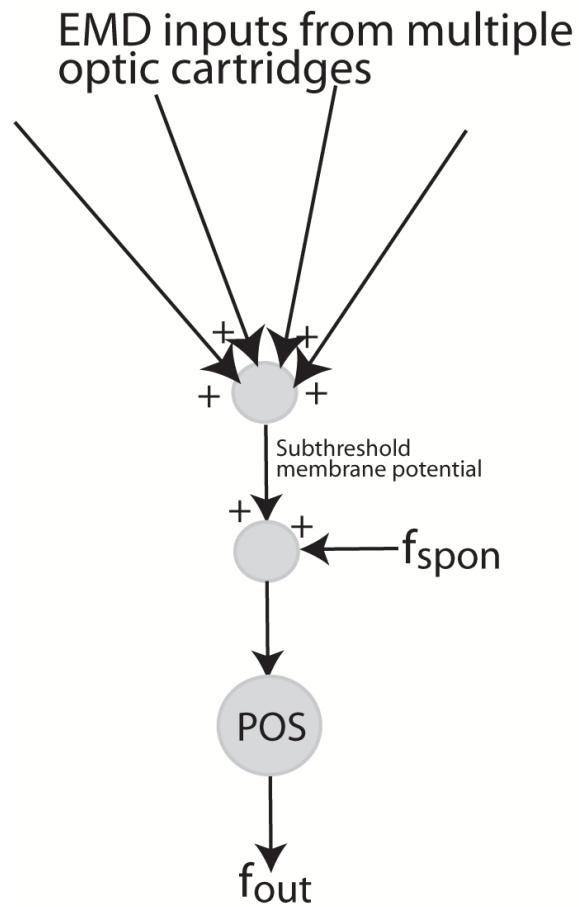
Figure 3.3: Integration of EMD model outputs of multiple optic cartridges into an LPTC as presented in Higgins et al. (2004). In addition to the spatial summation of multiple EMD outpus, the spontaneous firing rate (f_{spon}) is added before the signal is half-wave rectified (by the 'POS' operation), to produce the final LPTC output, f_{out}.

onset of the test stimulus (before and after adaptation) was recorded for each trial. A uniform stimulus was presented for at least 5 s between trials.

3.2   Results

Simulations of the Franceschini experiments have shown that our new model was able to demonstrate the following characteristics observed from the H1 cell responses in the same way as previous versions of the model. (1) When a single photoreceptor was presented with a flashing stimulus, no significant response was observed at the LPTC. (2) When two neighboring photoreceptors were each presented with a flashing stimulus simultaneously, no significant response was observed at the LPTC. (3) When two neighboring photoreceptors were each presented with a flashing stimulus sequentially, the LPTC showed directional selectivity. (4) The firing rate of the H1 cell when plotted against the delay time between the sequential flashings of two neighboring photoreceptors resembles the impulse response of a high-order low-pass filter. (5) The firing rate of the H1 cell when plotted against the delay time between the sequential sustained stimulations of two neighboring photoreceptors resembles the step response of a high-pass filter. Simulations of experiments from Egelhaaf and Borst (1989) have demonstrated that the tangential cell outputs oscillate at the temporal frequency of the input sinusoidal moving gratings due to transient responses of various temporal filters in the model. Lastly, when saltatory random gratings were presented to the model as done in Coombe et al. (1989), weak direction-selective responses were observed due to the relaxed high-pass filter implemented for the amacrine-T1 synapse which allows the passage of sustained luminance components. Results for all simulations described above were qualitatively comparable to those in Higgins et al. (2004) and therefore not included in the thesis.

We next investigated the effect which the temporal frequency and the pattern contrast of a motion stimulus had on the response of the simulated H1 cells in our revised model. Figure 3.4b shows the simulated H1 cell responses when first adapted
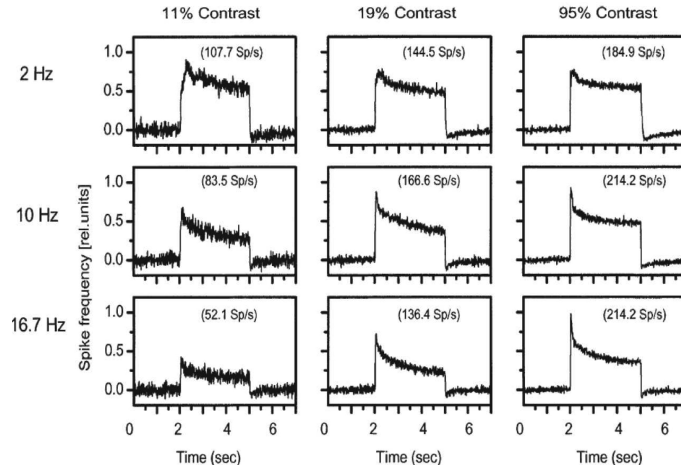
(a)
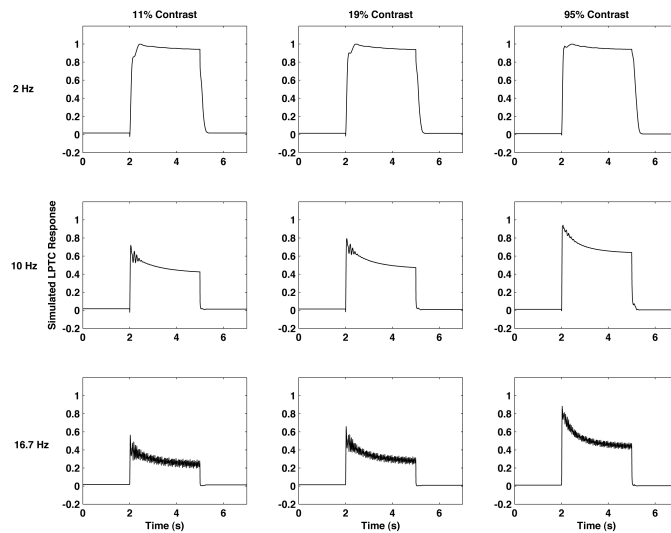
(b)

Figure 3.4: Adaptation during continuous preferred-direction motion stimulation. (a) Recorded responses from H1 cells as presented in Reisenman et al. (2003), reproduced without permission. (b) Simulated LPTC responses using the *revised* neuronally based EMD model. In both (a) and (b), the visual stimuli composed of 4 s of mean luminance and 3 s of a square-wave grating moving in the preferred direction. Three temporal frequencies (2 Hz, 10 Hz, and 16.7 Hz) and three pattern contrasts (11%, 19%, and 95%) were used. The results from (a) and (b) are qualitatively similar.

to 4 s of uniform stimulus before being presented with square-wave gratings moving in the preferred direction. Three temporal frequencies (2 Hz, 10 Hz, and 16.7 Hz) and three pattern contrasts (11%, 19%, and 95%) were used. Similar to experimental results from Reisenman et al. (2003), we made the following observations. (1) No transient oscillations were observed at the onset of motion when mean luminance instead of stationary grating was presented between trials, (2) the non-oscillatory transient responses decayed faster as both the temporal frequency and the pattern contrast increased, (3) optimal simulated H1 cell response was obtained at a temporal frequency of 2 Hz independent for all pattern contrast levels. When the depression gain factor D from the 'A' blocks in the model was plotted against time (Figure 3.5), we noticed a faster rate of adaptation as the temporal frequency and the pattern contrast of the test stimulus increased, reflecting the increase in transient response decay rate observed in the H1 cell recordings, allowing the simulated H1 cells to reach a steady-state level more rapidly.   We further tested the simulated H1 responses to test stimuli moving in the anti-preferred direction under the same protocol used for preferred-direction motion stimulation. The results are presented in Figure 3.6b and they exhibited all the same characteristics previously outlined for responses to preferred-direction motion. One thing worth noting was the presence of hyperpolarizing after-responses upon the cessation of the motion stimulus in the preferred direction, which was most notable in the case with a temporal frequency of 16.7 Hz and a pattern contrast of 0.11% (bottom-left window in Figure 3.4b). However, very little or no after-responses were observed upon the cessation of the motion stimulus in the anti-preferred direction. These findings were consistent with observations of LPTCs by Harris et al. (2000) and Kurtz et al. (2000).

Lastly, we investigated the effects of adaptation with motion in the preferred direction, motion in the anti-preferred direction, motion in the orthogonal direction, and wide-field flicker. Figure 3.7(a) shows the simulated HS cell responses to test stimuli of a range of pattern contrasts, before and after adaptation to motion in
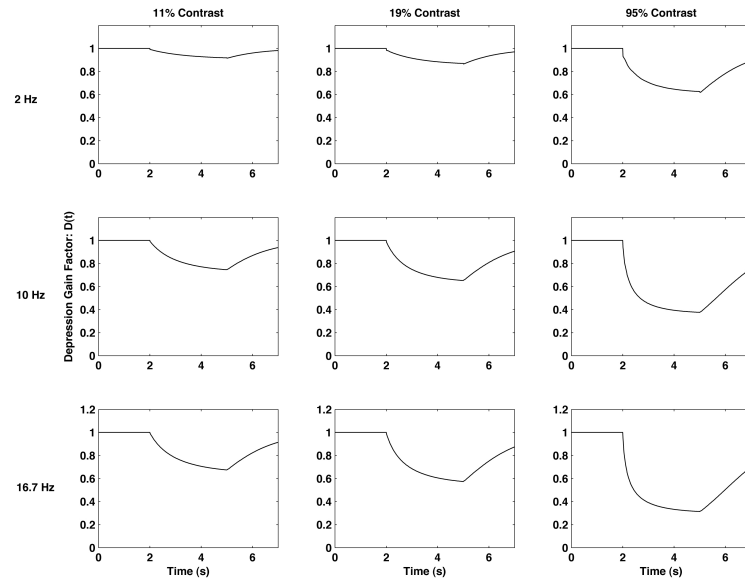
Figure 3.5: Depression gain factor $D(t)$ during continuous preferred-direction motion stimulation. The same stimulus protocol from Figure 3.4 was used. When the temporal frequency and the pattern contrast of the test stimulus increased, the rate of adaptation of the depression gain factor increased as well, allowing the cell to reach steady-state level quickly.
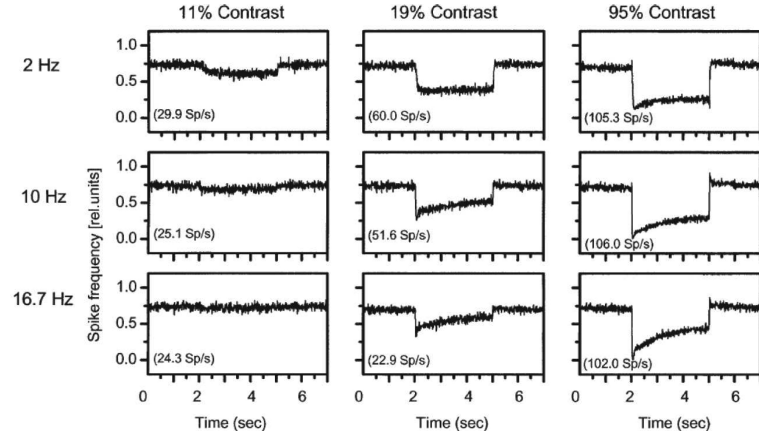
(a)
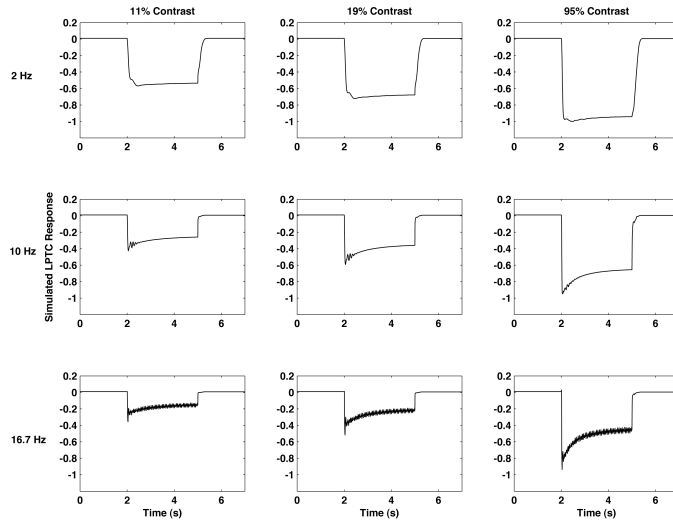
(b)

Figure 3.6: Adaptation during continuous anti-preferred-direction motion stimulation. (a) Recorded responses from H1 cells as presented in Reisenman et al. (2003), reproduced without permission. (b) Simulated LPTC responses using the *revised* neuronally based EMD model. In both (a) and (b), the visual stimuli composed of 4 s of mean luminance and 3 s of a square-wave grating moving in the anti-preferred direction. Three temporal frequencies (2 Hz, 10 Hz, and 16.7 Hz) and three pattern contrasts (11%, 19%, and 95%) were used. The results from (a) and (b) are qualitatively similar.
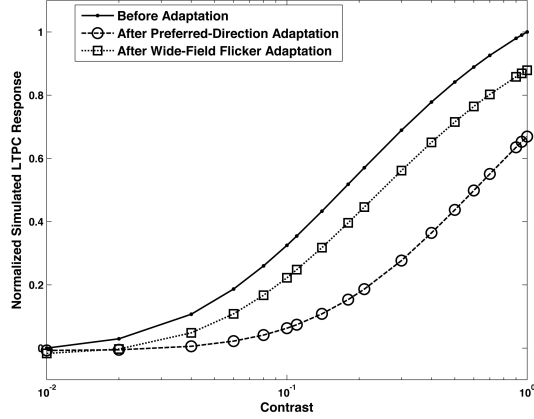
(a)
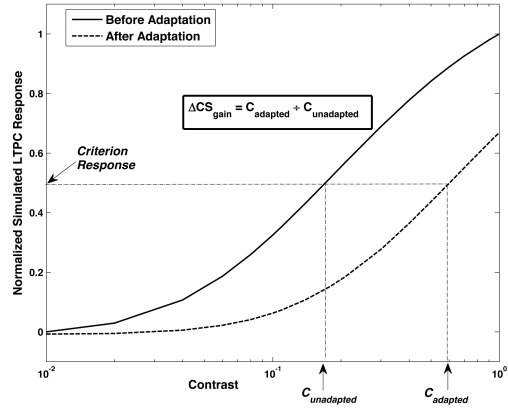
(b)

Figure 3.7: Simulated LPTC responses from adaptation to motion versus adaptation to flicker and protocol for calculating the contrast sensitivity of the simulated LPTC cell. (a) The preferred-direction motion adaptation produced approximately a 3.5-fold reduction in contrast sensitivity ($\Delta CS_{gain,10\%} = 3.48$ and $\Delta CS_{gain,50\%} = 3.51$) while the wide-field flicker produced approximately a 1.5-fold reduction in contrast sensitivity. (b) At a given criterion level (e.g. 10% or 50% of the maximum cell response), the pattern contrasts required to elicit this criterion response before and after the presentation of an adapting stimulus are denoted by $C_{unadapted}$ and $C_{adapted}$, respectively. The reduction in contrast sensitivity of the LPTC response is calculated by taking the ratio of $C_{adapted}$ to $C_{unadapted}$. Note that we are looking at only the changes resulting from the reduction in contrast gain, out of three motion adaptation features presented in Section 2.4.

the preferred direction and adaptation to wide-field flicker. As done in Harris et al. (2000), we evaluated the contrast that was required to elicit the 10% and 50% criterion response levels for each contrast-response curve, and determined the reduction in contrast sensitivity for each form of adaptation as illustrated in Figure 3.7(b). We found that the preferred-direction motion adaptation produced approximately a 3.5-fold reduction in contrast sensitivity ($\Delta CS_{gain,10\%} = 3.48$ and $\Delta CS_{gain,50\%} = 3.51$) while the wide-field flicker produced approximately a 1.5-fold reduction in contrast sensitivity. These values have been tuned using the parameter w in Equation 3.1 to match closely with the results from recorded electrophysiological data when the effect of the afterpotential was removed. The simulated mean LPTC response was determined between 200 ms and 500 ms following the onset of the test stimulus (before and after adaptation). Figure 3.8(a) shows the comparison between the contrast-response curves from adaptation with motion in the preferred direction and adaptation with motion in the anti-preferred direction. Motion in the anti-preferred direction induced a 3.5-fold reduction in contrast sensitivity ($\Delta CS_{gain,10\%} = 3.49$ and $\Delta CS_{gain,50\%} = 3.50$), comparable to the effect from adaptation to motion in the preferred direction. Consistent with results from Harris et al. (2000), adaptation to motion on average yielded a 3.5-fold reduction in contrast sensitivity regardless of the direction of motion. We further tested this by looking at the effect of adaptation to motion in the orthogonal direction (Figure 3.8b). We found that adaptation to motion in the orthogonal direction yielded a 3.53-fold reduction in contrast sensitivity ($\Delta CS_{gain,10\%} = 3.55$ and $\Delta CS_{gain,50\%} = 3.51$), which was slightly more than the effect of adaptation to preferred-direction motion. This has also been previously observed in HS cell recordings by Harris et al. (2000).

3.3   Summary and Discussion

In this revised neuronally based EMD model (Figure 3.2) two modifications were made to the elaborated neuronally based model by Rivera-Alvidrez (2005). First, a
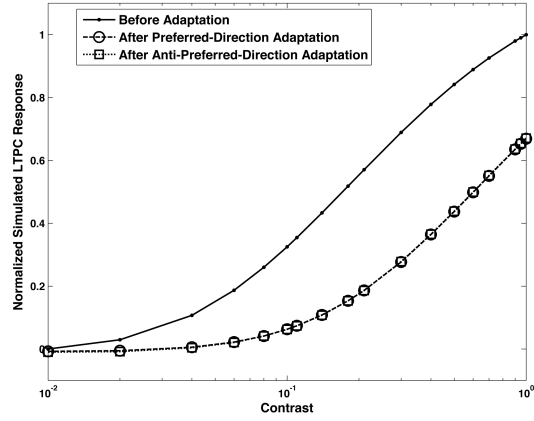
(a)
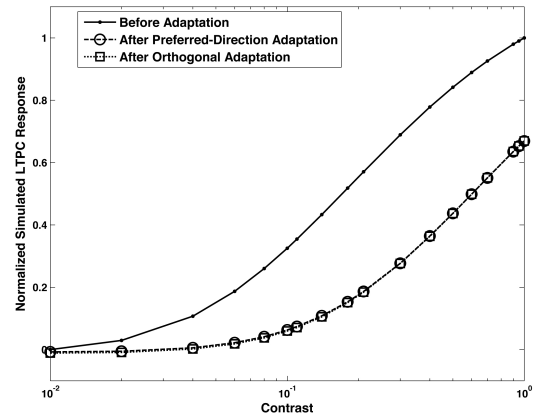
(b)

Figure 3.8: Simulated LPTC responses from adaptation to motion in the anti-preferred direction and from adaptation to motion in the orthogonal direction. (a) Motion in the anti-preferred direction induced a 3.5-fold reduction in contrast sensitivity ($\Delta CS_{gain,10\%} = 3.49$ and $\Delta CS_{gain,50\%} = 3.50$), same as the effect from adaptation to motion in the preferred direction. (b) Adaptation to motion in the orthogonal direction yielded a 3.53-fold reduction in contrast sensitivity ($\Delta CS_{gain,10\%} = 3.55$ and $\Delta CS_{gain,50\%} = 3.51$), slightly more than the effect of adaptation to preferred-direction motion. The simulated mean LPTC response was determined between 200 ms and 500 ms following the onset of the test stimulus (before and after adaptation) for both (a) and (b).

center-surround spatial filter was incorporated at the AM and L2 cell level to mimic the interaction between the AM1 cell and the AM2 cell networks, as well as the connections between the photoreceptor cells, the L2 cells, and the AM cells. Second, the computation of the shunting inhibition at the T5 level was revised to reflect the biophysics of synaptic processes between cells. The simulated cell responses from the model were able to match all the physiological cell responses exhibited by the two previous versions of the neuronally based EMD models.

The implementation of the center-surround spatial filter preserved motion information in the input signals while removing the majority of the spatial mean luminance from flickering stimuli. This allowed the model to produce simulated LPTC responses that reflect the motion adaptation characteristics not exhibited by the two previous neuronally based models. The most notable difference is the reduction in contrast sensitivity between the responses of a simulated LPTC cell after adaptation to motion stimuli and after adaptation to flickering stimuli. In Rivera-Alvidrez (2005) adaptation to motion stimuli and adaptation to flickering stimuli produced almost the same amount of reduction in contrast sensitivity. Our current model demonstrated that adaptation to motion stimuli produced approximately a 3.5-fold reduction in contrast sensitivity, while adaptation to wide-field flicker produced approximately only a 1.5-fold reduction. Furthermore, the current model was also able to show that adaptation to motion in any direction, including the anti-preferred and the orthogonal directions, elicited simulated LPTC responses with comparable, even identical, amounts of reduction in contrast sensitivity as observed by Harris et al. (2000) in real LPTC responses. By using the biophysical computation to represent the shunting inhibition taking place at the T5 cell level, the sigmoid function previously used in Rivera-Alvidrez (2005) to model contrast saturation could be eliminated.

Both the implementations of the center-surround spatial filter and the biophysical shunting computation contributed to making a more realistic neuronally based

58

EMD model, as well as producing simulated LPTC outputs that exhibited motion adaptation responses which are a closer match to those observed in real LPTCs.

The work described in this chapter has been prepared into a draft manuscript for journal publication. This manuscript can be found in Appendix A.

CHAPTER 4

Optics and Photoreceptor Modeling

Previous neuronally-based EMD models sampled and inserted light information directly at the level of photoreceptor cell outputs, neglecting possible pre-processing of light information taking place at the optics level and the photoreceptor level. In this thesis we describe the additions of two newer stages – the optics of the compound eye and the photoreceptor model – to the revised neuronally-based EMD model from Chapter 3 for a more complete and realistic model of the insect visual pathway.

Features of the compound eye optics are important for navigational tasks in a real-world environment. The acute zones (see Section 2.2.1) allow for higher visual acuity when viewing fast-moving objects, which is important for target tracking behaviors such as foraging. The lateral regions of the compound eye with relatively sparse ommatidial distribution are more tuned to objects moving at lower speeds, essential for stabilization against the moving background during flight. We constructed a realistic three-dimensional compound eye using geometrical data measured from a blowfly in previous studies (Petrowitz et al., 2000). We also implemented the Gaussian blurring which results from the interaction between light and the optical structure of the lenses on the compound eye.

The pre-processed light information from the optics stage is relayed to the next stage: the photoreceptor model. We based our photoreceptor implementation on the work of van Hateren and Snippe (2001). Their model is shown in Figure 4.1 and consists of two divisive feedback loops and a static nonlinearity. The first divisive feedback loop is referred to as the De Vries-Rose model and exhibits steady-state input-output behavior such that the output is the square-root of the input. It
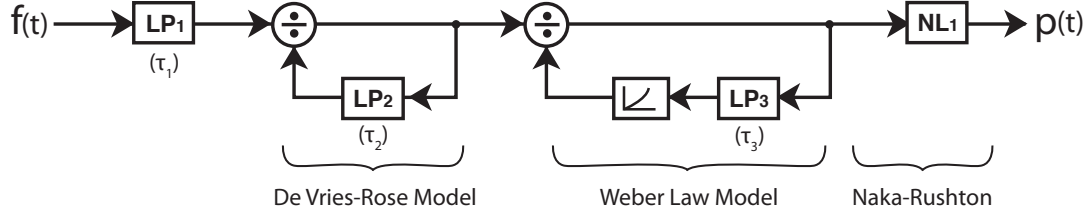
Figure 4.1: Photoreceptor model from van Hateren and Snippe (2001). This model consists of two divisive feedback loops and a static nonlinearity, referred to as the De Vries-Rose model, the Weber Law model, and the Naka-Rushton equation, respectively. The three modules work together to compress large transients in the input stimulus into the dynamic range of the photoreceptor cells. $f(t)$ and $p(t)$ respectively denote the input and the output of the model.

produces overshoots and undershoots during increments and decrements of light intensity, respectively, as a result of the presence of the low-pass filter. The second divisive feedback loop is referred to as the Weber Law model (Dehaene, 2003) and exhibits steady-state input-output behavior such that the output is the logarithm of the input. When presented with light intensity steps, the output of this loop shows a slow decrease in response following a fast transient response. The last component of this photoreceptor model is implemented as a Naka-Rushton equation (Naka and Rushton, 1966):

$$o = \frac{i}{(1+i)} \tag{4.1}$$

where i and o respectively denote the input and the output of this component of the model. This nonlinearity is used to compress any remaining responses that are outside of the dynamic range of the photoreceptors.
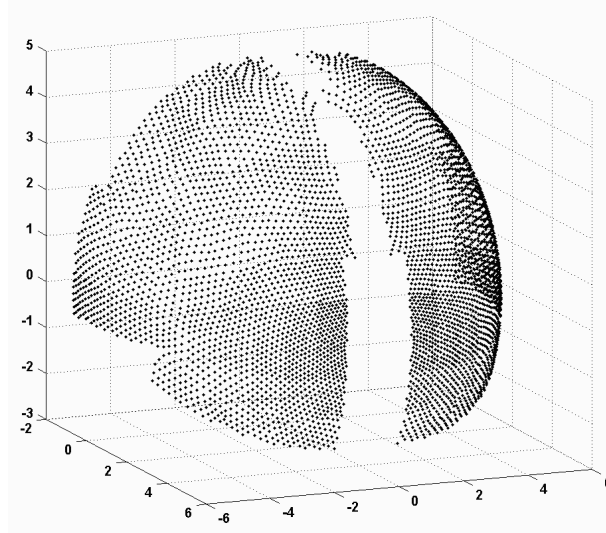
Figure 4.2: Reconstructed three-dimensional compound eyes of a female *Calliphora*. The azimuth and elevation angles recorded by Petrowitz et al. (2000) are used to plot the location of each ommatidium on two spheres of a radius of 5 mm. Each ommatidium is represented by a dot in the image. The left and the right compound eyes are mirror images of each other.

4.1   Methods

An image containing measured optical axes of ommatidia on the compound eye of female house fly *Calliphora* was obtained from Petrowitz et al. (2000). A program was written in *Matlab* (The Mathworks, Natick, MA) to extract and store the azimuth and elevation angles of each optical axis plotted on this map. We also defined the radius of the compound eye to be 5 mm and generated the Cartesian coordinates to represent the locations of the ommatidia. This information was used to re-construct a three-dimensional compound eye with realistic ommatidial distribution (Figure 4.2). For each ommatidium we identified its six nearest neighboring ommatidia (Figure 4.3), whose input signals would later be used for motion computation within the EMD model.

When presenting a visual stimulus, we positioned the stimulus such that the
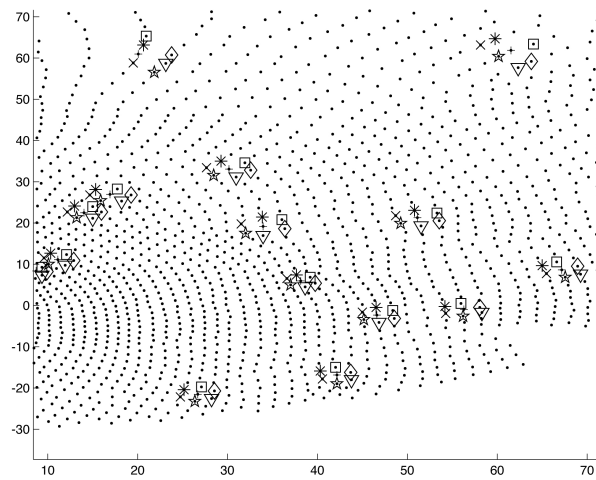
Figure 4.3: Locating the nearest six neighboring ommatidia for each individual ommatidium on the compound eye. This image demonstrates how the Matlab code written was able to locate the six neighboring ommatidia and their relative positions to each *center* ommatidium. The operation was performed on all 2386 ommatidia of a single compound eye. In each group of seven ommatidia, the *center* one is denoted by a cross ($+$), the *upper-left* neighbor is denoted by an asterisk ($*$), the *upper-right* neighbor is denoted by a square ($\square$), the *right* neighbor is denoted by a diamond ($\diamond$), the *lower-right* neighbor is denoted by a triangle ($\triangledown$), the *lower-left* neighbor is denoted by a star ($\star$), and the *left* neighbor is denoted by an '$\times$'.
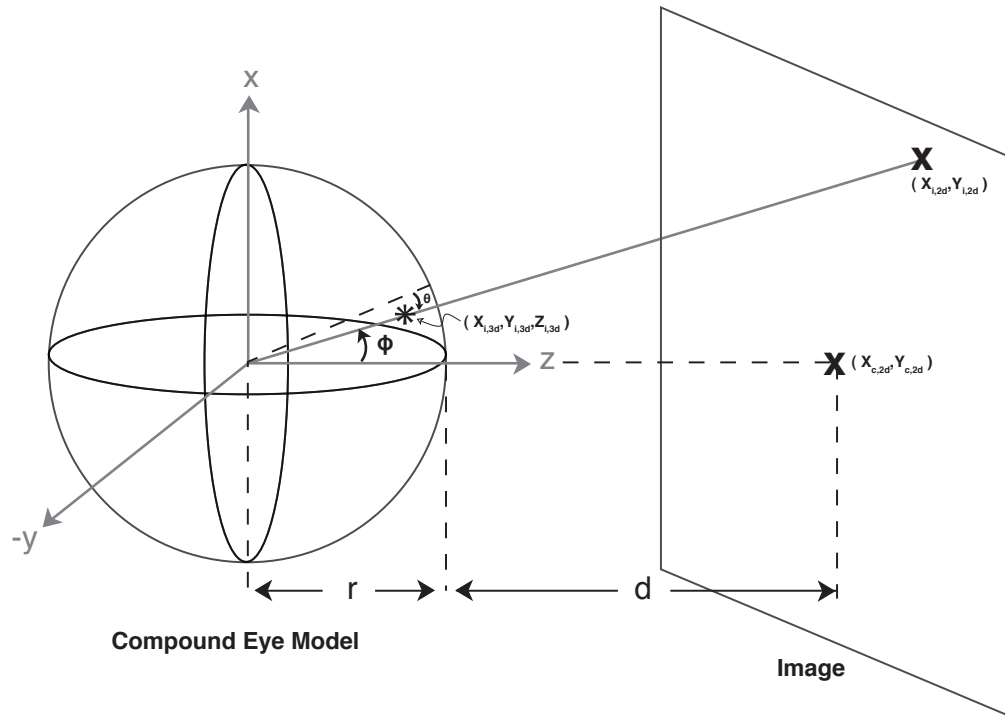
Figure 4.4: Virtual setup of the three-dimensional compound eye and the visual stimulus. The center of the visual image, $(x_{c,2d}, y_{c,2d})$, is aligned with the optical axis on the three-dimensional compound eye model with an azimuth angle and an elevation angle of $0°$ (i.e. the z-axis in this setup). The projected two-dimensional location on the visual image being sampled by the ommatidium denoted by '$*$' (three-dimensional coordinate $(x_{i,3d}, y_{i,3d}, z_{i,3d})$) is marked by an $\times$ (two-dimensional coordinate $(x_{i,2d}, y_{i,2d})$). r is the radius of the eye, d is the distance of the visual image from the eye, θ and ϕ are the elevation angle and the azimuth angle representing the ommatidium '$*$', respectively.

center of the image was aligned with the optical axis of the three-dimensional compound eye model with an azimuth angle and an elevation angle of $0°$ (Figure 4.4). To determine the two-dimensional location on the visual image being sampled by each ommatidium we derived Equation 4.2:

$$\begin{cases} x_{i,2d} = x_{c,2d} + \frac{d \cdot x_{i,3d}}{z_{i,3d}} \\ y_{i,2d} = y_{c,2d} + \frac{d \cdot y_{i,3d}}{z_{i,3d}} \end{cases} \tag{4.2}$$

where $(x_{i,2d}, y_{i,2d})$ is the two-dimensional location on the visual image being sampled by the ith ommatidium, $(x_{c,2d}, y_{c,2d})$ is the location of the center of the image, d (set to be 8 cm in the simulations) is the distance of the two-dimensional visual image from the three-dimensional compound eye, and $(x_{i,3d}, y_{i,3d}, z_{i,3d})$ is the three-dimensional location of the ith ommatidium.

We next modeled the Gaussian blurring effect inherent in the optics of the fly compound eye. At the output of the optics stage, the signal at each ommatidial location represents the average of the local signal and the weighted signals from all neighboring ommatidia within a range programmed to enclose approximately five layers of neighbors. For each ommatidium there were n_i neighboring ommatidia being enclosed in the pre-defined area on the compound eye. The signal f_i from the ith ommaditium at the output of the optics stage was computed using Equation 4.3 which represents a Gaussian function:

$$f_i = \frac{1}{(1 + n_i)} \times \left[s_i + \sum_{j=1}^{n_i} s_j \times e^{\frac{(x_{i,2d} - x_{ij,2d})^2 + (y_{i,2d} - y_{ij,2d})^2}{2\sigma^2}} \right] \tag{4.3}$$

where s_i is the sampled signal by the ith ommaditium, $(x_{ij,2d}, y_{ij,2d})$ is the location on the visual image sampled by the jth neighboring ommatidium of the ith ommatidium, and σ is the standard deviation of the Gaussian distribution.

The photoreceptor stage was modeled based on the implementation by van Hateren and Snippe (2001) with the following parameters from Higgins (2011). LP_1 was set as a third-order low-pass filter with $\tau_1 = 0.5$ ms. In the De Vries-Rose model

LP$_2$ was set to be a first-order low-pass filter with $\tau_2 = 0.4$ s. In the Weber Law model, LP$_3$ was set as a first-order low-pass filter with $\tau_3 = 10$ s and the input-output behavior of the exponential block was set as $o = 3.7e^i$. Lastly the 1 in the Naka-Rushton equation (Equation 4.1) was replaced with a 0.75.

All the simulations were carried out using the revised EMD model from Chapter 3 *with* the addition of the optics stage and the photoreceptor stage. The simulated T5 cell responses were compared to and contrasted against those from the revised EMD model *without* the optics stage and the photoreceptor stage. The drifting sinusoidal grating stimulus used in all the simulations is described by Equation 4.4:

$$I(x, y, t) = B \left(1 + C \cdot sin(w_t \cdot t + w_s \cdot s + \phi)\right) \qquad (4.4)$$

where B is the background luminance, C is the pattern contrast, w_t is the temporal frequency, w_s is the spatial frequency, and ϕ is the initial phase.

4.2   Results

The revised EMD model with the optics/photoreceptor addition was presented with a moving sinusoidal grating that moved in the preferred direction for 2.5 s before changing to the anti-preferred direction for 2.5 s. B, C, w_t, w_s, and ϕ of the stimulus were each set to 0.5 unit, 50%, 15 Hz, 0.225 cycles/optic cartridge, and 0 radians, respectively. This stimulus as viewed by an arbitrarily chosen visual sampling unit is shown in the upper-right panel of Figure 4.5(a). After being processed by the optics stage and the photoreceptor stage, the amplitude of this stimulus was drastically reduced from 0.5 unit to 0.04 unit (*upper-left* panel). Additionally, the resulting simulated T5 cell response (*lower-left* panel) was found to be more directionally-sensitive, as evident in the greater difference observed between the mean T5 cell response to motion in opposite directions, compared to the response elicited by the model *without* the optics/photoreceptor addition (*lower-right* panel). Similar observations were made when a moving square-wave grating was used as a test

stimulus (Figure 4.5b).

Next, the background luminance B of the visual stimulus was varied over five orders of magnitude between 0.5 units and 5×10^3 units. As shown in Figure 4.6, the background luminance of a sinusoidal moving grating was 0.5 units for the first 3 s, then was increased to 50 units for 3 s, before being increased again to 5×10^3 units. The sinusoidal grating moved in the preferred direction for 1 s before changing to the anti-preferred direction for 1 s. Regardless of how big the background luminance was, the photoreceptor stage was able to compress all of the input signals into an amplitude between 0 and 1 unit.

Finally, we looked at the simulated T5 cell responses when our current model was subject to a visual stimulus with a very high or a very low background luminance. Figure 4.7(a) shows the simulated T5 cell response of both the current model with (*lower-left* panel) and without the optics and photoreceptor stage (*lower-right* panel), to a visual stimulus with a pattern contrast of 50% and a background luminance of 5×10^4 units. The sinusoidal grating moved in the preferred direction for 2.5 s before changing to the anti-preferred direction for 2.5 s. It was observed that without the proper signal compression from the optics and photoreceptor stage, propagation of large signals within the EMD model resulted in undesirable artifacts evident in the flat-lining of the simulated T5 cell response (*lower-right* panel of Figure 4.7(a)). The artifacts were found to originate from the 'A' blocks which model the frequency-dependent synaptic depression at the TM1 cell level. Since the operation of this synaptic depression uses the absolute values of the input signals for amplitude reduction, the speed of adaptation (i.e. amplitude reduction) increases drastically when the values of the inputs are very large.

Figure 4.7(b) shows the simulated T5 cell response of both the current model with (*lower-left* panel) and without the optics and photoreceptor stage (*lower-right* panel), to a visual stimulus with a pattern contrast of 50% and a background luminance of 5×10^{-3} units. The sinusoidal grating moved in the preferred direction for
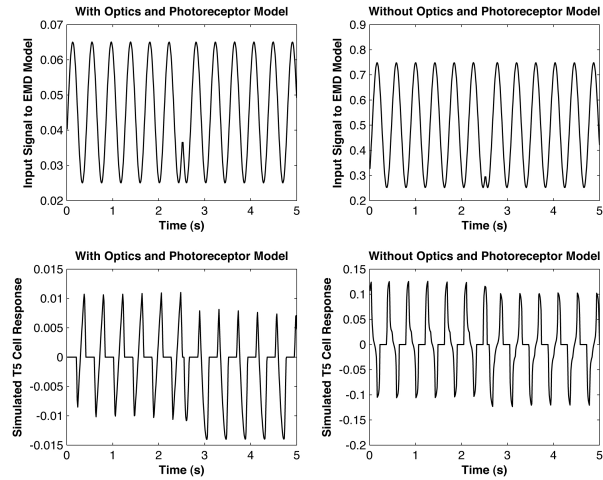
(a)
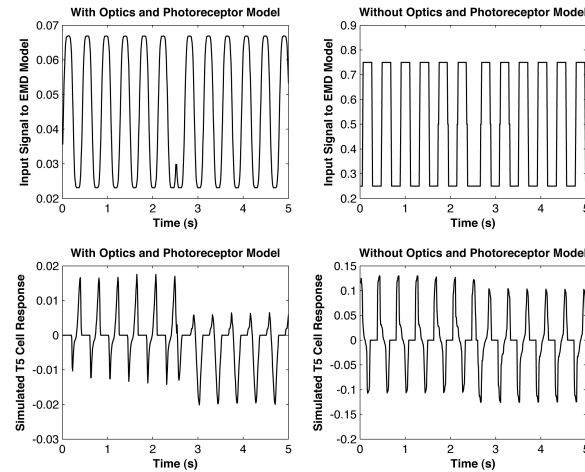
(b)

Figure 4.5: Simulated T5 cell responses of the revised EMD model with and without the optics and photoreceptor stage. (a) After being processed by the optics stage and the photoreceptor stage, the amplitude of a moving sinusoidal grating was drastically reduced (*upper-left* panel) and the directional selectivity of the simulated T5 cell response was enhanced (*lower-left* panel) compared that of the model without the optics and photoreceptor model (*lower-right* panel). (b) Similar results were obtained when a moving square-wave grating was used as a visual stimulus.
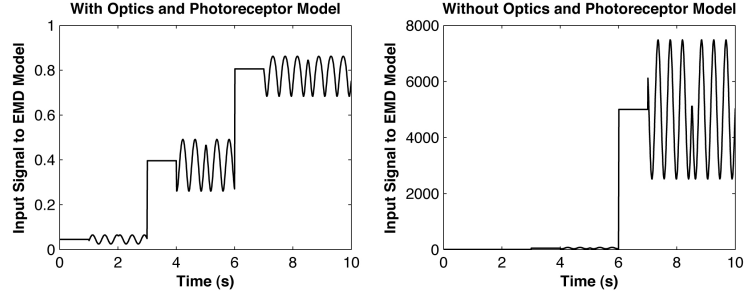
Figure 4.6: Photoreceptor cell responses to visual stimulus with changing background luminance. The background luminance of a sinusoidal moving grating was 0.5 unit for the first 3 s, then was increased to 50 units for 3 s, before being increased again to 5×10^3 units. The photoreceptor stage was able to compress signals with large amplitudes into an amplitude of 0 to 1, while preserving the transient information.

2.5 s before changing to the anti-preferred direction for 2.5 s. The model without the optics and photoreceptor stage was found to produce simulated T5 cell responses that started to lose directional selectivity as the input signals became very small. The very same effect was observed from the model with the optics and photoreceptor stage, however with more deterioration.

When visual stimuli of a background luminance in the range of 5×10^{-3} and 5×10^4 were presented, both the model with and without the optics and photoreceptor stage performed well. Both exhibited directional selectivity similar to that shown in Figure 4.5, with the former showing a greater difference between the mean T5 cell response to motion in opposite directions.

4.3   Summary and Discussion

The previous neuronally-based model assumed a uniform field of view, such that every region in the visual field was viewed by the same number of sampling units (i.e. ommatidia). Through the implementation of the realistic ommatidial distribution in this section, each area on the compound eye was populated with different densities
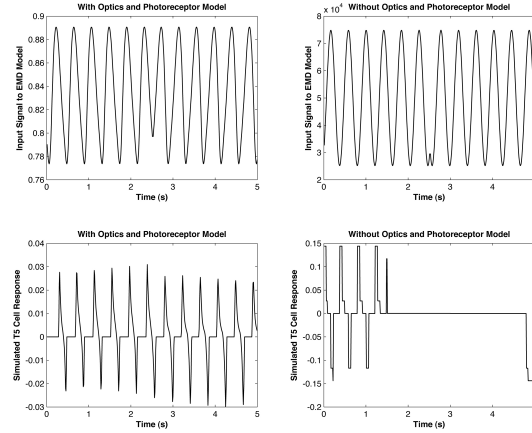
(a)
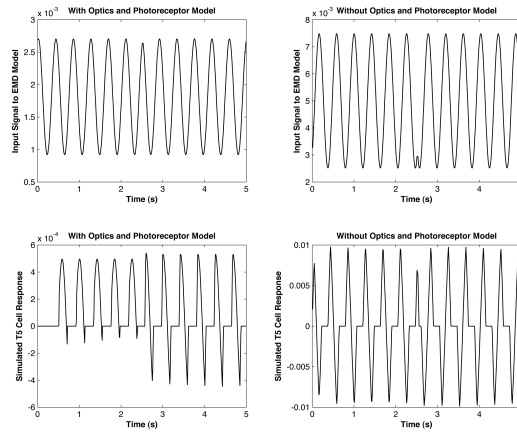
(b)

Figure 4.7: Simulated T5 cell responses to a moving sinusoidal grating with high background luminance and with low background luminance. (a) When a stimulus with a high background luminance of 5×10^4 units was used, the model with the optics and photoreceptor stage was still fully functional (*lower-left* panel) as a result of proper signal compression (*upper-left* panel), while the model without the optics and photoreceptor stage encountered undesirable artifacts evident in the flat-lining of the simulated T5 cell response (*lower-right* panel). (b) When a stimulus with a low background luminance of 5×10^{-3} units was used, the further compression of an already small signal (*upper-left* panel) from the photoreceptor model resulted in deterioration of the simulated T5 response observed at the output of the model with the optics and photoreceptor model (*lower-left* panel), while the model without the optics and photoreceptor stage fared better even though it did start losing its directional selectivity (*lower-right* panel).

of ommatidia depending on the type of visual stimulus it is specialized to view. As discussed in Section 2.2.1, the frontal area is specialized for accurately tracking small targets, and therefore requires the use of more sampling units. On the other hand, the lateral regions are more loosely populated with sampling units in comparison, because the motion of the background experienced during forward flight is generally of less importance. The use of a non-uniform ommatidial distribution allowed a smaller number of pixels to be used in regions outside of the acute zone, therefore lowering the computational burden imposed on the EMD model. Although the true advantages of using a realistic compound eye model were not demonstrated in this thesis, the eye model will be extremely useful for future work with simulations in a closed-loop environment.

The photoreceptor stage was able to reduce the amplitude of the input signals, as is evident from Figures 4.5 to 4.7. The logarithmic function in the Weber Law model reduced the effect of the changing background luminance and coded for the pattern contrast of the visual stimulus. This pre-processing of the input signals allowed the EMD model to perform optimally even when presented with background luminance over a wide range of values as shown in Figure 4.6, by compressing the input signals into a realistic range of cellular potentials exhibited by neurons. Nevertheless, a disadvantage of the photoreceptor model was evident when visual stimuli of low background luminance were used. Since even small signals that might already be in the dynamic range of the photoreceptor cells are further compressed regardless of their size, small input signals can become miniscule after being processed by the photoreceptor model. This can cause deterioration of the EMD model output as evident in Figure 4.7(b).

CHAPTER 5

Summary and Future Work

In this thesis, three additions were incorporated into the elaborated neuronally-based motion-detecting model by Rivera-Alvidrez (2005). The implementation of the center-surround spatial filters and the biophysical shunting inhibition function described in Chapter 3 allowed the model to produce simulated LPTC responses that exhibit motion adaptation characteristics which are a closer match to recorded LPTC data compared to the previous two versions of the neuronally-based model. Our current model demonstrated that adaptation to motion stimuli produced a significantly greater reduction in contrast sensitivity, compared with adaptation to wide-field flicker. In addition it also showed that adaptation to motion in any direction, including the anti-preferred and the orthogonal directions, elicited simulated LPTC responses with comparable, even identical, amounts of reduction in contrast sensitivity as observed by Harris et al. (2000) in real LPTC responses.

The implementation of the optics and photoreceptor stage emulated how light information is processed in a real compound eye. The realistic ommatidial distribution reflected the specialization of each area of the eye to view different types of visual stimuli. The frontal area is populated with more sampling units for accurate tracking of small targets, while the lateral regions are more loosely populated for viewing motion of the background experienced during forward flight. The photoreceptor model compressed the input signals into a realistic range of cellular potentials exhibited by neurons, which allowed the EMD model to perform well even when presented with background luminance over a wide range of values.

5.1 Future Work

The amount of saturation observed in the contrast response curves in Chapter 3 did not quite match that from Harris et al. (2000), even when the biophysical shunting inhibition is implemented in place of the sigmoid function. Future work might include a closer examination at the neuronally-based model to locate a physiologically sound site to implement computational modules that will achieve this.

Additionally, due to time constraints, we were not able to fully explore the advantages of the optics stage implementation or the photoreceptor model in Chapter 4. Future work may include the use of more realistic visual stimuli as seen by a fly and the use of a closed-loop simulation environment.

5.2 Contributions of the Author

The formulation of the center-surround spatial filter was performed by the author in collaboration with Dr. Charles M. Higgins. The implementation of the center-surround spatial filters into the EMD model and subsequent simulations were carried out by the author. The Matlab code for biophysical shunting inhibition was devloped by Lise Johnson, and later tuned and implemented in the EMD model by the author.

The incorporation of the realistic compound eye model was performed by the author of this thesis, including all Matlab coding, simulations, and mathematical derivations, using data from Petrowitz et al. (2000) kindly provided by Dr. Holger G. Krapp. The photoreceptor model was implemented by the author using the mathematical model from van Hateren and Snippe (2001), with the assistance of Dr. Charles M. Higgins in tuning the model parameters.

REFERENCES

Adelson, E. H. and J. R. Bergen (1985). Spatiotemporal energy models for the perception of motion. *Journal of the Optical Society of America A*, **2**(2), pp. 284–299.

Barlow, H. and W. Levick (1965). The mechanism of directionally selective units in rabbit's retina. *The Journal of Physiology*, **178**(3), pp. 477–504.

Beersma, D. G. M., D. G. Stavenga, and J. W. Kuiper (1977). Retinal lattice, visual field and binocularities in flies. *Journal of Comparative Physiology A: Neuroethology, Sensory, Neural, and Behavioral Physiology*, **119**(3), pp. 207–220.

Borst, A. Borst, Haag, and J. Haag (2002). Neural networks in the cockpit of the fly. *Journal of Comparative Physiology A: Neuroethology, Sensory, Neural, and Behavioral Physiology*, **188**(6), pp. 419–437.

Borst, A. and M. Dickinson (2003). Visual course control in flies. In *The Handbook of Brain Theory*, pp. 1205–1210. Bradford Books/MIT Press, USA.

Borst, A. and M. Egelhaaf (1989). Principles of visual motion detection. *Trends in Neurosciences*, **12**(8), pp. 297–306.

Borst, A., M. Egelhaaf, and J. Haag (1995). Mechanisms of dendritic integration underlying gain control in fly motion-sensitive interneurons. *Journal of Computational Neuroscience*, **2**(1), pp. 5–18.

Braddick, O. J., K. H. Ruddock, M. J. Morgan, and D. Marr (1980). Low-Level and High-Level Processes in Apparent Motion [and Discussion]. *Philosophical Transactions of the Royal Society of London. B, Biological Sciences*, **290**(1038), pp. 137–151.

Brenner, N. (2000). Adaptive Rescaling Maximizes Information Transmission. *Neuron*, **26**(3), pp. 695–702. ISSN 08966273.

Buchner, E. (1984). Behavioural analysis of spatial vision in insects. In *Photoreception and vision in invertebrates*, pp. 561–622. Plenum, New York.

Buchner, E., S. Buchner, and R. Hengstenberg (1979). 2-Deoxy-D-glucose maps movement-specific nervous activity in the second visual ganglion of Drosophila. *Science*, **205**(4407), pp. 687–688. ISSN 0036-8075.

Campos-Ortega, J. and N. Strausfeld (1973). Synaptic connections of intrinsic cells and basket arborizations in the external plexiform layer of the fly's eye. *Brain Research*, **59**, pp. 119–136. ISSN 0006-8993.

Collett, T. and M. Land (1978). How hoverflies compute interception courses. *Journal of Comparative Physiology A: Neuroethology, Sensory, Neural, and Behavioral Physiology*, **125**(3), pp. 191–204.

Coombe, P. E., M. V. Srinivasan, and R. G. Guy (1989). Are the large monopolar cells of the insect lamina on the optomotor pathway? *Journal of Comparative Physiology A: Neuroethology, Sensory, Neural, and Behavioral Physiology*, **166**(1), pp. 23–35.

Dehaene, S. (2003). The neural basis of the Weber-Fechner law: a logarithmic mental number line. *Trends in Cognitive Sciences*, **7**(4), pp. 145–147. ISSN 1364-6613.

Douglass, J. and N. Strausfeld (1995). Visual motion detection circuits in flies: peripheral motion computation by identified small-field retinotopic neurons. *J. Neurosci.*, **15**(8), pp. 5596–5611.

Douglass, J. K. and N. J. Strausfeld (2005). Sign-Conserving Amacrine Neurons in the Fly's External Plexiform Layer. *Visual Neuroscience*, **22**(03), pp. 345–358.

Eckert, H. and D. R. Dvorak (1983). The centrifugal horizontal cells in the lobula plate of the blowfly, Phaenicia sericata. *Journal of Insect Physiology*, **29**(7), pp. 547–553, 555–560. ISSN 0022-1910.

Egelhaaf, M. and A. Borst (1989). Transient and steady-state response properties of movement detectors. *Journal of the Optical Society of America A*, **6**(1), pp. 116–127.

Egelhaaf, M. and A. Borst (1993). A look into the cockpit of the fly: visual orientation, algorithms, and identified neurons. *The Journal of Neuroscience: The Official Journal of the Society for Neuroscience*, **13**(11), pp. 4563–4574. ISSN 0270-6474. PMID: 8229185.

Franceschini, N., A. Riehle, and A. Le Nestour (1989). Directionally selective motion detection by insect neurons. In *Facets of Vision*, pp. 360–390. Springer-Verlag, Heidelberg, New York.

Groombridge, B. (1992). *Global biodiversity : status of the earth's living resources : a report*. Chapman & Hall, London ; New York :. ISBN 0412472406.

Hardie, R. C. (1985). Functional organization of the fly retina. In *Progress in sensory physiology*, volume 5, pp. 1–79. Springer.

Hardie, R. C. (2001). Phototransduction in Drosophila melanogaster. *J Exp Biol*, **204**(20), pp. 3403–3409.

Harris, R. A. and D. C. O'Carroll (2002). Afterimages in fly motion vision. *Vision Research*, **42**(14), pp. 1701–1714. ISSN 0042-6989.

Harris, R. A., D. C. O'Carroll, and S. B. Laughlin (2000). Contrast Gain Reduction in Fly Motion Adaptation. *Neuron*, **28**(2), pp. 595–606. ISSN 08966273.

Hassenstein, B. and W. Reichardt (1956). Systemtheoretische Analyse der Zeit-, Reihenfolgen- und Vorzeichenauswertung bei der Bewegungsperzeption des Rsselkfers Chlorophanus. *Zeitschrift für Naturforschung B*, **11**(9), pp. 513–524.

Hausen, K. (1982). Motion sensitive interneurons in the optomotor system of the fly. *Biological Cybernetics*, **45**(2), pp. 143–156.

Hausen, K. (1984). The lobula-complex of the fly: structure, function and significance in visual behaviour. In *Photoreception and vision in invertebrates*. Plenum Press.

Hengstenberg, R. (1982). Common visual response properties of giant vertical cells in the lobula plate of the blowflyCalliphora. *Journal of Comparative Physiology A: Neuroethology, Sensory, Neural, and Behavioral Physiology*, **149**(2), pp. 179–193.

Higgins, C. (2011). Reverse Engineering the Fly. In Preparation.

Higgins, C., J. Douglass, and N. Strausfeld (2004). The Computational Basis of an Identified Neuronal Circuit for Elementary Motion Detection in Dipterous Insects. *Visual Neuroscience*, **21**(04), pp. 567–586.

Hooke, R. (1665). *Micrographia*. Royal Society of London. ISBN 9781426486760.

Horn, B. K. and B. G. Schunck (1981). Determining optical flow. *Artificial Intelligence*, **17**(1-3), pp. 185–203. ISSN 0004-3702.

Hubel, D. and M. Livingstone (1987). Segregation of form, color, and stereopsis in primate area 18. *J. Neurosci.*, **7**(11), pp. 3378–3415.

Jarvilehto, M. and F. Zettler (1971). Localized intracellular potentials from pre- and postsynaptic components in the external plexiform layer of an insect retina. *Journal of Comparative Physiology A: Neuroethology, Sensory, Neural, and Behavioral Physiology*, **75**(4), pp. 422–440.

Juusola, M., E. Kouvalainen, and M. Weckstrm (1994). Contrast gain, signal-to-noise ratio, and linearity in light-adapted blowfly photoreceptors. *Journal of General Physiology*, **104**, pp. 593—621.

Kirschfeld, K. and N. Franceschini (1968). Optische Eigenschaften der Ommatidien im Komplexauge von Musca. *Biological Cybernetics*, **5**(2), pp. 47–52.

Koch, C. (1999). *Biophysics of Computation: Information Processing in Single Neurons (Computational Neuroscience Series)*. Oxford University Press, Inc. ISBN 0195181999.

Kohn, A. and J. Movshon (2003). Neuronal Adaptation to Visual Motion in Area MT of the Macaque. *Neuron*, **39**(4), pp. 681–691. ISSN 08966273.

Kramer, J., R. Sarpeshkar, and C. Koch (1997). Pulse-Based Analog VLSI Velocity Sensors.

Kurtz, R., V. Durr, and M. Egelhaaf (2000). Dendritic Calcium Accumulation Associated With Direction-Selective Adaptation in Visual Motion-Sensitive Neurons In Vivo. *J Neurophysiol*, **84**(4), pp. 1914–1923.

Land, M. F. (1981). Optics and vision in invertebrates. In *Handbook of sensory physiology*, volume 7, pp. 471–592. Springer-Verlag.

Land, M. F. (1997). Visual Acuity in Insects. *Annual Review of Entomology*, **42**(1), pp. 147–177. ISSN 0066-4170.

Land, M. F. and T. S. Collett (1974). Chasing behaviour of houseflies (Fannia canicularis). *Journal of Comparative Physiology A: Neuroethology, Sensory, Neural, and Behavioral Physiology*, **89**(4), pp. 331–357.

Land, M. F. and H. Eckert (1985). Maps of the acute zones of fly eyes. *Journal of Comparative Physiology A: Neuroethology, Sensory, Neural, and Behavioral Physiology*, **156**(4), pp. 525–538.

Land, M. F. and D. Nilsson (2002). *Animal eyes*. Oxford University Press. ISBN 9780198509684.

Laughlin, S. B., J. Howard, and B. Blakeslee (1987). Synaptic limitations to contrast coding in the retina of the blowfly Calliphora. *Proceedings of the Royal Society of London. Series B, Containing Papers of a Biological Character. Royal Society (Great Britain)*, **231**(1265). ISSN 0080-4649.

Limb, J. and J. Murphy (1975). Estimating the Velocity of Moving Images in Television Signals. *Computer Graphics and Image Processing*, **4**(4), pp. 311–327. ISSN 0146-664X.

Maddess, T. (1986). Afterimage-Like Effects in the Motion-Sensitive Neuron H1. *Proceedings of the Royal Society of London. Series B. Biological Sciences*, **228**(1253), pp. 433–459.

Maddess, T. and S. B. Laughlin (1985). Adaptation of the Motion-Sensitive Neuron H1 is Generated Locally and Governed by Contrast Frequency. *Proceedings of the Royal Society of London. Series B. Biological Sciences*, **225**(1239), pp. 251–275.

Marr, D. and S. Ullman (1981). Directional Selectivity and its Use in Early Visual Processing. *Proceedings of the Royal Society of London. Series B, Biological Sciences*, **211**(1183), pp. 151–180. ISSN 00804649.

Naka, K. I. and W. A. H. Rushton (1966). S-potentials from colour units in the retina of fish (Cyprinidae). *The Journal of Physiology*, **185**(3), pp. 536–555.

Nakayama, K. (1985). Biological image motion processing: A review. *Vision Research*, **25**(5), pp. 625–660. ISSN 00426989.

Nakayama, K. and G. H. Silverman (1988). The aperture problem–I. Perception of nonrigidity and motion direction in translating sinusoidal lines. *Vision Research*, **28**(6), pp. 739–746. ISSN 0042-6989.

Olberg, R. M., A. H. Worthington, and K. R. Venator (2000). Prey pursuit and interception in dragonflies. *Journal of Comparative Physiology A: Neuroethology, Sensory, Neural, and Behavioral Physiology*, **186**(2), pp. 155–162.

Petrowitz, R., H. Dahmen, M. Egelhaaf, and H. G. Krapp (2000). Arrangement of optical axes and spatial resolution in the compound eye of the female blowfly Calliphora. *Journal of Comparative Physiology A: Neuroethology, Sensory, Neural, and Behavioral Physiology*, **186**(7), pp. 737–746.

Poggio, T. and W. Reichardt (1973). Considerations on models of movement detection. *Biological Cybernetics*, **13**(4), pp. 223–227.

Reichardt, W. (1987). Evaluation of optical motion information by movement detectors. *Journal of Comparative Physiology A: Neuroethology, Sensory, Neural, and Behavioral Physiology*, **161**(4), pp. 533–547.

Reisenman, C., J. Haag, and A. Borst (2003). Adaptation of response transients in fly motion vision. I: Experiments. *Vision Research*, **43**(11), pp. 1291–1307. ISSN 0042-6989. PMID: 12726835.

Rivera-Alvidrez, Z. (2005). *Computational Modeling of Neurons Involved in Fly Motion Detection*. Master's thesis, The University of Arizona.

Rivera-Alvidrez, Z. and C. M. Higgins (2005). Contrast saturation in a neuronally-based model of elementary motion detection. *Neurocomputing*, **65-66**, pp. 173–179. ISSN 0925-2312.

Sinakevitch, I. and N. J. Strausfeld (2004). Chemical neuroanatomy of the fly's movement detection pathway. *The Journal of Comparative Neurology*, **468**(1), pp. 6–23. ISSN 0021-9967.

Single, S., J. Haag, and A. Borst (1997). Dendritic Computation of Direction Selectivity and Gain Control in Visual Interneurons. *J. Neurosci.*, **17**(16), pp. 6023–6030.

Srinivasan, M. (1990). Generalized gradient schemes for the measurement of two-dimensional image motion. *Biological Cybernetics*, **63**(6), pp. 421–431.

Srinivasan, M. and D. Dvorak (1979). The waterfall illusion in an insect visual system. *Vision Research*, **19**(12), pp. 1435–1437. ISSN 0042-6989.

Srinivasan, M. V., S. B. Laughlin, and A. Dubs (1982). Predictive Coding: A Fresh View of Inhibition in the Retina. *Proceedings of the Royal Society of London. Series B, Biological Sciences*, **216**(1205), pp. 427–459. ISSN 00804649. Article-Type: primary_article / Full publication date: Nov. 22, 1982 / Copyright 1982 The Royal Society.

Srinivasan, M. V., M. Lehrer, W. H. Kirchner, and S. W. Zhang (1991). Range perception through apparent image speed in freely flying honeybees. *Visual Neuroscience*, **6**(5), pp. 519–535. ISSN 0952-5238.

Strausfeld, N. and D. Nässel (1981). Neuroarchitectures serving compound eyes of Crustacea and insects. In *Handbook of sensory physiology*, pp. 1–132. Springer.

Strausfeld, N. J. (1976). *Atlas of an Insect Brain*. Springer. ISBN 0387073434.

Strausfeld, N. J. and J. K. Lee (1991). Neuronal basis for parallel visual processing in the fly. *Visual Neuroscience*, **7**(1-2), pp. 13–33. ISSN 0952-5238.

Tix, S., E. Eule, K. Fischbach, and S. Benzer (1997). Glia in the chiasms and medulla of the Drosophila melanogaster optic lobes. *Cell and Tissue Research*, **289**(3), pp. 397–409.

Tomasi, C. and T. Kanade (1991). Detection and Tracking of Point Features. *International Journal of Computer Vision*, **9**, pp. 137—154.

Tootell, R. B. H., J. B. Reppas, A. M. Dale, R. B. Look, M. I. Sereno, R. Malach, T. J. Brady, and B. R. Rosen (1995). Visual motion aftereffect in human cortical area MT revealed by functional magnetic resonance imaging. *Nature*, **375**(6527), pp. 139–141.

van Hateren, J. H. and H. P. Snippe (2001). Information theoretical evaluation of parametric models of gain control in blowfly photoreceptor cells. *Vision Research*, **41**, pp. 1851–1865.

van Santen, J. P. H. and G. Sperling (1984). Temporal covariance model of human motion perception. *Journal of the Optical Society of America A*, **1**(5), pp. 451–473.

van Santen, J. P. H. and G. Sperling (1985). Elaborated Reichardt detectors. *Journal of the Optical Society of America A*, **2**(2), pp. 300–320.

Yamaguchi, S., R. Wolf, C. Desplan, and M. Heisenberg (2008). Motion vision is independent of color in Drosophila. *Proceedings of the National Academy of Sciences*, **105**(12), pp. 4910–4915. ISSN 0027-8424.

APPENDIX A

A Neuronally-Based Model of Contrast Gain Adaptation in Fly Motion Vision.

Zuley Rivera-Alvidrez, Ichi Lin and Charles M. Higgins

In preparation for submission to

Visual Neuroscience